UNIVERSITY OF OKLAHOMA

GRADUATE COLLEGE

3D FINITE ELEMENT MODELING OF BLAST WAVE TRANSMISSION IN
HUMAN EAR FROM EXTERNAL EAR TO COCHLEAR HAIR CELLS

A THESIS

SUBMITTED TO THE GRADUATE FACULTY

in partial fulfillment of the requirements for the

Degree of

MASTER OF SCIENCE

By

JOHN BRADSHAW

Norman, Oklahoma

2023

3D FINITE ELEMENT MODELING OF BLAST WAVE TRANSMISSION IN
HUMAN EAR FROM EXTERNAL EAR TO COCHLEAR HAIR CELLS

A THESIS APPROVED FOR THE
STEPHENSON SCHOOL OF BIOMEDICAL ENGINEERING

BY THE COMMITTEE CONSISTING OF

Dr. Rong Z. Gan, Chair

Dr. Chenkai Dai

Dr. Michael S. Detamore

Acknowledgments

This thesis would have been impossible without the support and guidance of the members of the Biomedical Engineering Lab. My advisor, Dr. Rong Gan, has constantly provided valuable advice and pushed me to accomplish high-quality research for all the years I worked in her lab. Her wisdom and experience were an inspiration to me as I performed my own research. I would not be as good of an engineer without Dr. Gan, and I will be eternally grateful for her mentorship. I am very appreciative of all the help I received from Marcus Brown: he taught me how to work with the finite element model and gave me practical and moral support when I struggled with modeling projects. I would also like to thank Shangyuan Jiang, who consistently offered me help and made working in the lab very enjoyable.

I must also thank Dr. Xuelin Wang for his expertise in finite element analysis and hard work in constructing and meshing the organ of Corti model.

I am thankful for all the work other students and researchers have put into the finite element model of the ear over the years, and I am proud to have pushed the project even further.

I would like to express my gratitude to my committee members, Dr. Chenkai Dai and Dr. Michael Detamore, for the time and effort they have dedicated to helping me complete my degree and the advice they have provided me during my time at OU.

And lastly, I offer my thanks to my parents, Jack and Janet Bradshaw, for all the support they have offered me during my degree. I am truly grateful for the love you have given me.

Table of Contents

List of Tables

List of Figures

Abstract

Auditory system dysfunction caused by exposure to blast waves is one of the leading causes of disability among military servicemembers and veterans. While the external and middle ear response to blast overpressures (BOPs) have been characterized experimentally, the inner ear behavior is much more difficult to measure, especially the micro-level cochlear hair cells in the organ of Corti (OC) responsible for converting pressure waves into electrical signals. Recently, computational finite element (FE) models have advanced to predict blast wave transmission from the external ear into the cochlea. However, in published FE models the anatomy of the inner ear is still insufficient. The objective of this study was to develop a 3D FE model of the human ear that included a 3-chambered cochlea to improve inner ear anatomy, validate the model's results, and simulate the behavior of the OC during blast wave transmission.

The human ear FE model consists of the ear canal, middle ear, and spiral cochlea with 3 chambers (scala vestibuli, scala media, and scala tympani) separated by Reissner's membrane (RM) and the basilar membrane (BM). The model was run as a coupled fluid-structural analysis in ANSYS. An experimentally recorded blast waveform was applied as input to the entrance of the ear canal, and the model outputs included the ear canal (P_1) and cochlear pressures, and the displacements of the tympanic membrane (TM), stapes footplate (SFP), and BM. The results of the model were compared to experimental measurements from blast tests in order to validate the FE model's results. In addition, a microscale structural model of the OC was developed that used the FE model-derived BM displacement at 16.75 mm

from the BM base end as input. This model reported some preliminary results describing the motion of the outer hair cells (OHCs) and hair bundles (HBs).

The FE model of the human ear successfully predicted the middle and inner ear tissue displacements and fluid pressures. The P_1 pressure, cochlear pressures, TM displacement, and SFP displacements were validated against blast test results. The incorporation of the 3-chambered cochlea improved the model's accuracy compared to previous cochlea models used for blast transmission and demonstrated the influence of the RM and scala media chamber on cochlear biomechanics. These results were used to predict the likelihood of auditory injury. In addition, the preliminary results of the OC model showed radial variation in the OHC and HB behavior and indicated some potential mechanisms of sensory hair cell injury.

The FE model reported in this thesis successfully improved the simulation of human cochlear anatomy and was validated against experimental blast measurements. A microscale model of the OC was connected with the full human ear model, giving some preliminary insight into blast-induced OC behavior. Future work with this model will improve the connection between the cochlea model and OC model and apply the FE model of the human ear to hearing loss prediction and the evaluation of earplug effectiveness.

Chapter 1: Introduction

1.1 Motivation

The daily functioning and mental state of military servicemembers and veterans are commonly hindered by auditory system disabilities. In the fiscal year 2022, 2.7 million veterans received compensation for tinnitus, and 1.4 million received compensation for hearing loss[1]; together, they are the most common service-connected disabilities reported among veterans. Hearing loss is strongly associated with decreased military operational performance,[2,3] lower speech comprehension in noisy environments,[4] and reduced quality of life.[5]

Blast-exposed military personnel have a significantly higher risk of ear injury and hearing loss.[6,7] Blast overpressures (BOPs) are high-intensity disturbances in the ambient air pressure[8] that generally over 170 dB SPL. BOPs induce extreme deformation of the tympanic membrane (TM) and significant movement of the stapes footplate (SFP) when compared to those caused by normal sound[9,10]. TM rupture, middle ear ossicular chain disruption, and cochlea hair cell damage are commonly reported as blast-induced hearing injury in the literature[9–13]. Military servicemembers are commonly exposed to BOPs generated by artillery, gunfire, and explosions, so an understanding of the mechanisms of blast-induced hearing loss is important. The behavior of the external and middle ear during blast exposure is well-documented[9,10] but the reported data from the inner ear response is significantly more limited.

Computational finite-element (FE) models have been utilized to analyze pressure transmission through the ear. FE modeling provides a valuable tool for predicting the inner ear behavior that is otherwise difficult to measure experimentally, including the motion of the basilar membrane (BM) and hair cells in the organ of Corti (OC). The development of

an FE model simulating these components is essential to gaining a full understanding of the effect of BOP transmission in the inner ear.

1.2 Peripheral Auditory System

This thesis is primarily concerned with the peripheral auditory system (PAS). The PAS detects pressure waves and transmits them through the ear until they are converted into nervous signals sent into the central auditory system (CAS). The ear is commonly divided into the external ear, middle ear, and inner ear.

The external ear starts at the auricle, which funnels sound and pressure waves into the ear canal. The ear canal transmits sound waves to the TM, or eardrum. The middle ear consists of the TM, manubrium, ossicles and suspensory ligaments. The TM is connected to the ossicular chain by the manubrium, and the TM vibrations induced by sound waves in the ear canal cause the ossicles to move. The ossicular chain is comprised of, in order, the malleus, incus, and stapes. The SFP presses against the oval window membrane (OWM) of the inner ear and serves as the primary input into the inner ear. The basic anatomy of the human ear is displayed in **Fig. 1**.
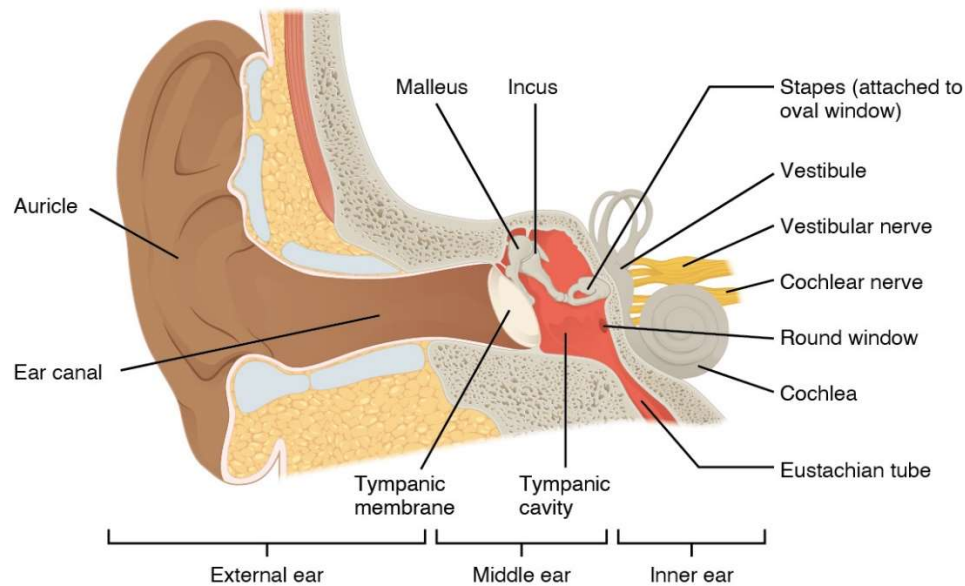
Figure 1. The anatomy of the human ear, with the external, middle, and inner ear labelled. (https://openstax.org/books/anatomy-and-physiology/pages/14-1-sensory-perception)

The inner ear is fluid-filled and includes the semicircular canals and the cochlea. The cochlea contains three chambers—the scala vestibuli (SV), which connects to the OWM, the scala media (SM), separated from the other chambers, and the scala tympani (ST), which contacts the round window membrane (RWM)—separated by Reissner's membrane (RM) and the basilar membrane (BM), respectively. The RM is a thin, flexible membrane spanning the width of the cochlea, and the BM is thin and stiff near the base of the cochlea, and wide and flexible near the apex. The SV and ST are connected by the helicotrema, located at the cochlear apex. The SFP motion generates pressure waves in the inner ear fluid, which travel through the cochlea and displace the BM.

The OC is located on the BM in the SM. The organ consists of 3 rows of outer hair cells (OHCs) and 1 row of inner hair cells (IHCs), supported by Dieters' cells (DCs) and phalangeal processes (PhPs). The OC structure is supported by outer and inner pillar cells (OPCs and IPCs, respectively), Hensen's cells (HCs), and the osseous spiral lamina of the

3

cochlea. Stereocilia connected to the hair cells are arranged into rows of increasing length and extend between the reticular lamina (RL) and tectorial membrane (TcM). **Figure 2** provides cross-sectional view of the cochlea and the OC. The OC detects pressure waves in the cochlea via the bending of the stereocilia, which cause the mechanosensory hair cells to send nervous signals to the auditory nerve and CAS. The BM is tuned via its mechanical and structural properties so that high frequency sounds are processed by the basal hair cells, and low frequency sounds are processed by the apical hair cells.

1.3 Finite Element Models of the Human Ear

The FE modeling handles complex geometries by subdividing them into discrete finite elements. This mesh model is governed by a set of differential equations approximating the mechanics of the simulated system. FE analysis is well-suited to the middle ear and inner ear structures, and many studies have developed FE models of the human ear for a variety of applications. Several acoustic and blast wave transmission models were relevant to the development of the model detailed in this thesis.
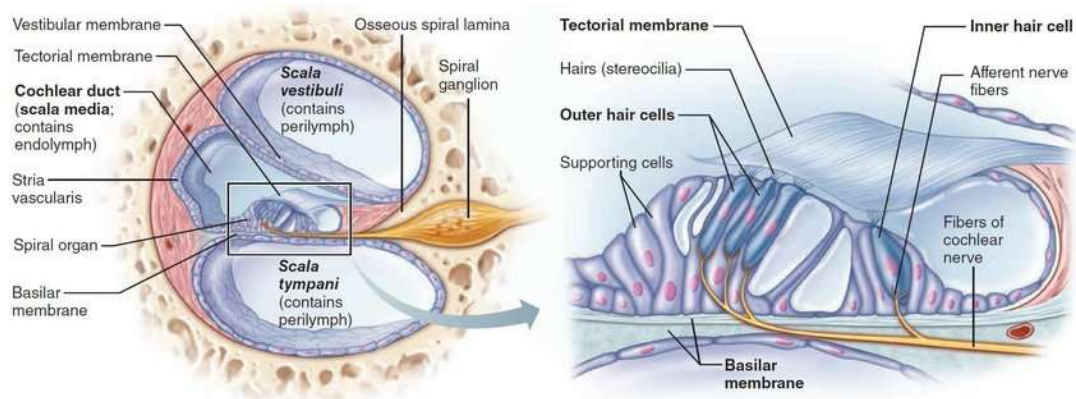
Figure 2. Cross-section view of the human cochlea with the OC enlarged. The OC is located in the SM, between the RM and BM, and is responsible for converting pressure waves in the cochlea into electrical signals sent into the CAS. (https://www.researchgate.net/figure/Cross-section-of-the-cochlea-with-enlarged-organ-of-Corti-40_fig1_330111901)

4

1.3.1 Sound Transmission Through the Ear

Many 3D finite element (FE) models of the cochlea have been published in the literature for acoustic sound transmission[14–21]. Böhnke and Arnold[14] published one of the earliest FE models of the 2-chambered cochlea to predict the basilar membrane displacement. The first FE model of the entire human ear including the external ear, middle ear with the cavity, and two-chamber straight cochlea for sound transmission from the ear canal to the cochlea was reported by Gan et al. (2007).[22] This study built on the model described in Gan et al. (2004),[23] which used 3D reconstruction technology based on histological section images of a human temporal bone (TB) to construct the geometry of the ear canal and middle ear tissues. Finally, an FE model of the human ear with a spiral-shaped 3-chambered cochlea was published by Zhang and Gan[16,17], shown in **Fig. 3**, and used in the study of hearing devices and energy absorbance in normal and disordered human ears. All of these FE models were used for the simulation of normal sound transmission through the ear at the frequency domain and could not predict the transient behavior of the ear.
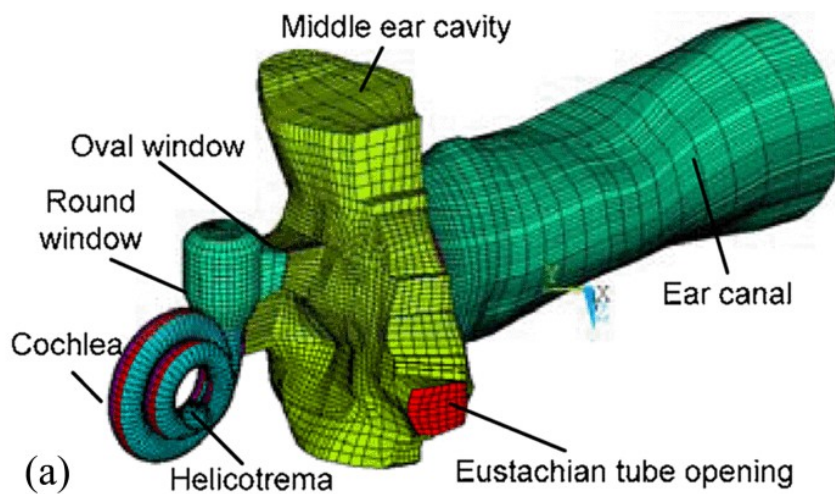
Figure 3. The FE model described by Zhang and Gan (2011). This model ran a frequency-domain analysis of acoustic pressure transmission and provides the structure of the cochlea used in later blast wave transmission models.

1.3.2 Blast Wave Transmission Through the Ear

Leckness et al.[24] reported the first 3D FE model used to simulate the blast wave transmission through the ear, consisting of the ear canal, middle ear with the cavity, and cochlear load represented by a mass block-dashpot system. Using experimentally measured blast waveforms in human TBs, the results from this FE model reflected the pressures observed throughout the ear and the stress distribution within the TM which were comparable to measured pressures and TM damage examination in TBs. This model was the first transient FE analysis of blast wave transmission through the ear conducted using a coupled fluid-structure setup, and was subsequently applied to an analysis of the effectiveness of earplugs for attenuating BOPs.[16] Following Leckness et al.'s FE model, the 3D FE model of the entire ear with 2-chambered straight cochlea was first developed by Brown et al. (2021)[20] to predict the significant displacements of the TM, middle ear ossicles, and cochlear basilar membrane. Then, the straight cochlea model was improved to the 2-chambered spiral cochlea of two and a half turns described in Brown et al. (2022)[21] and shown in **Fig. 4**. The spiral shape of the cochlea caused an asymmetric pressure distribution across the width of the cochlea or the cochlea chambers and allowed for significant transverse motion of the BM. This model also assessed auditory injury markers using the FE model-derived results.
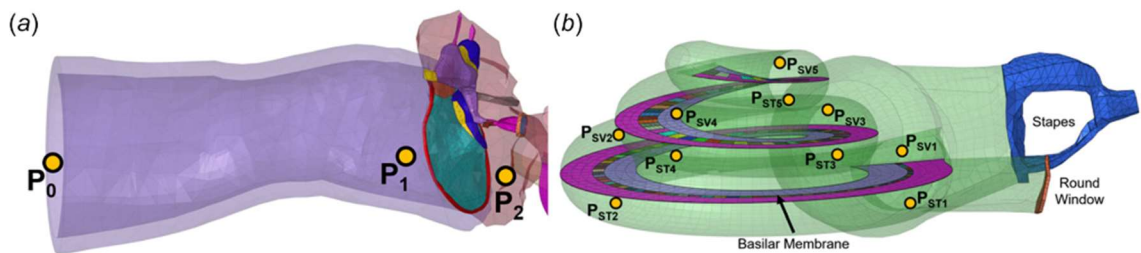
Figure 4. The FE model of the human ear described in Brown et al. (2022). This model simulated blast wave transmission and utilized a 2-chambered cochlea with a BM, but no RM or SM. The intracochlear pressures were predicted with this model.

These models confirmed that BOPs induced higher tissue displacements than normal sound exposure and reported that injury in the middle ear and cochlea were likely. The blast model were results validated against experimental blast tests,[20,21,24] demonstrating the success of coupled fluid-structure analyses for simulating transient, high-deformation biomechanical problems. However, the state of these blast models still leaves room for improvements to the anatomical accuracy of the cochlea and the addition of smaller structures such as the OC.

1.3.3 Organ of Corti & Cochlear Hair Cells

The OC is important for the translation of pressure in the cochlea into nervous signals traveling into the central auditory system. Understanding the mechanics of the OC is key to determining the differences in OC behavior from the cochlear base to apex and determining the mechanisms through which inner ear injuries occur. Several FE models of the OC have been published.

Ramamoorthy et al.[25] described the first 3D FE model of the OC that was incorporated into a straight, 2-chambered gerbil cochlea. The mechano-electro-acoustic model included the fluid in the cochlea and the piezoelectric behavior of the OHCs, and used a radial modal decomposition to improve the model's computational efficiency. The OC structure was simplified and included the BM, OHCs, pillar cells, RL, TcM, and stereociliar hair bundles (HBs). This model was expanded in Meaud and Grosh,[26] which added viscoelastic longitudinal coupling to the BM and TcM components. A detailed, 3D FE mechanical model of the OC was described in Zagadou et al. (2014).[27] In addition to the inner and outer sensory hair cells, the model included more supporting cells of the OC than previous models and was used in an inverse analysis of the elastic material properties

of the OC components. In 2019, Sasmal and Grosh[28] presented a more detailed OC model, displayed in **Fig. 5**, that they used to examine the effect of the SV and ST structure of the cochlea on the OC behavior. Their model supported the claim that the spatial variation along the length of the cochlea influenced the high and low frequency tuning of the cochlea.

These models are excellent examples of the development and application of 3D FE models of the OC. However, some gaps in the literature on OC modeling are clear. No FE models predicting OC behavior during blast wave transmission have been published. Furthermore, the integration of OC models with cochlea models is limited to straight, 2-chambered gerbil cochleae. An FE model of the human OC, paired with a spiral-shaped, 3-chambered human cochlea, is needed to better understand the effect of blast wave transmission on the human inner ear.
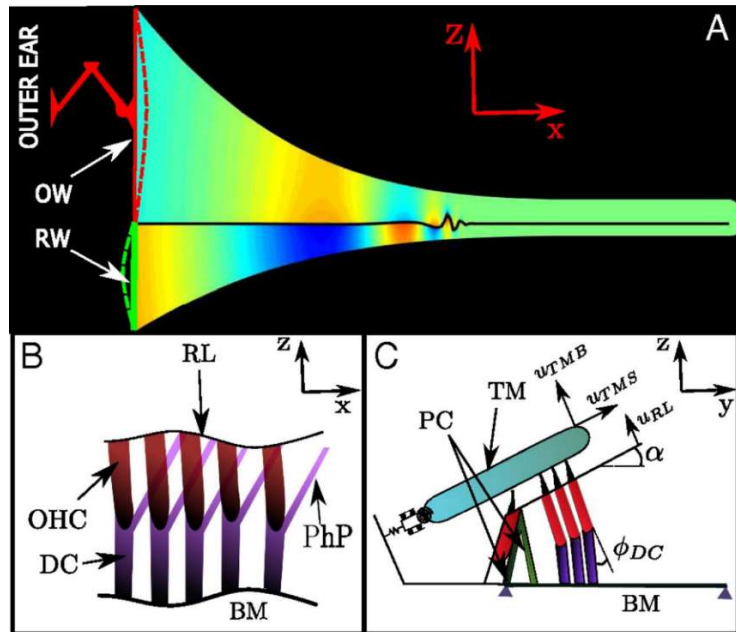
Figure 5. The unified cochlea-OC FE model reported in Sasmal and Grosh (2019). This model consisted of a simple 2-chambered gerbil cochlea (a) and a 5-row OC model (b) containing the OC's membranes, sensory hair cells, and supporting cells. The models were unified to simulate low- and high-frequency hearing.

1.4 Objectives

In order to better understand and reliably predict hearing loss and injury in the human ear resulting from BOP exposure, improved and models of the human ear are required. 3D FE computational modeling is the best tool for simulating the 3D behavior of the middle and inner ear with geometry accurate to the ear's anatomy. In order to advance the understanding of ear biomechanics during blast wave transmission, a multiscale FE model of the human ear was developed, consisting of a macroscale model of the human ear and a microscale model of the human OC. This model is the most comprehensive FE model of the ear, further improving the anatomy of the inner ear and integrating the OC, which will provide useful results for understanding how the behavior of the OC during blast leads to hearing loss. The FE model can also be used to predict the effectiveness of hearing protection devices (HPDs) or the likelihood of injury resulting from theoretical blast waveforms. The goal of this study is to further advance the understanding of auditory blast injury and provide a useful tool for predicting the likelihood of hearing loss.

Chapter 2: 3D Finite Element Analysis of Blast Wave Transmission through Human Ear Model

2.1 Creation of the 3D Finite Element Model of Human Ear

2.1.1 Macroscale Human Ear Model

The 3D FE macroscale model of the human ear with a 3-chamber spiral cochlea was built based on the model reported by Brown et al.[21] The model consists of the external ear canal, middle ear, and spiral cochlea. The middle ear includes the TM, which is connected by the manubrium to the three ossicles (malleus, incus, and stapes). The ossicles are connected together by the incudomalleolar joint (IMJ) and ISJ and suspended in middle ear cavity by ligaments and muscle tendons (C1 to C7). The spiral cochlea has two and a half turns and connects to the middle ear at the oval window through the SFP and stapedial annular ligament (SAL) and at the round window through the RWM as shown in **Figs. 6(a)** and **6(b)**. **Figure 6(a)** displays the posterior view of the model with the middle ear cavity partially transparent to show the ossicles and **Fig. 6(b)** is a magnified view of the connections between the middle ear and cochlea, showing the basilar membrane inside the cochlea. The P_0 and P_1 marked in **Fig. 6(a)** represent the locations where input pressure P_0 was applied to the model and the ear canal pressure P_1 near the TM derived from the model, respectively.

The spiral cochlea has three fluid-filled chambers: the SV, SM, and ST, separated by the RM and the BM as illustrated in **Figs. 6(c)** and **6(d)**. **Figure 6(c)** gives a transparent view of the cochlea with the connection to the SFP and RWM and marks the location of P_{SV}, the point where SFP-adjacent cochlear pressure is measured. The BM and RM extend the full length of the cochlea's spiral turns. The BM has a width that increases from 0.13 mm to 0.50 mm and is flanked by a supporting bony lamina, while the RM width does not

vary significantly. The SV connects to the ST at the helicotrema, as shown in **Fig. 6(c)**, while the SM is disconnected from the rest of the cochlear fluid. **Fig. 6(d)** provides a cross-sectional view of the three chambers of the cochlea and clearly shows that the SM lies between the SV and ST.

All structural components including middle ear ossicles and soft tissues, the air in the ear canal and middle ear cavity, and the fluid inside the cochlea were meshed using Hypermesh software (Altair Engineering, Inc., Troy, MI), the same methods reported in previous FE models[17,20–22,24]. The BM and RM are composed of hexahedral elements, while the remaining structural components and fluids are made of tetrahedral and pyramidal elements. The structural and fluid models consist of 16,343 and 170,383 elements, respectively.
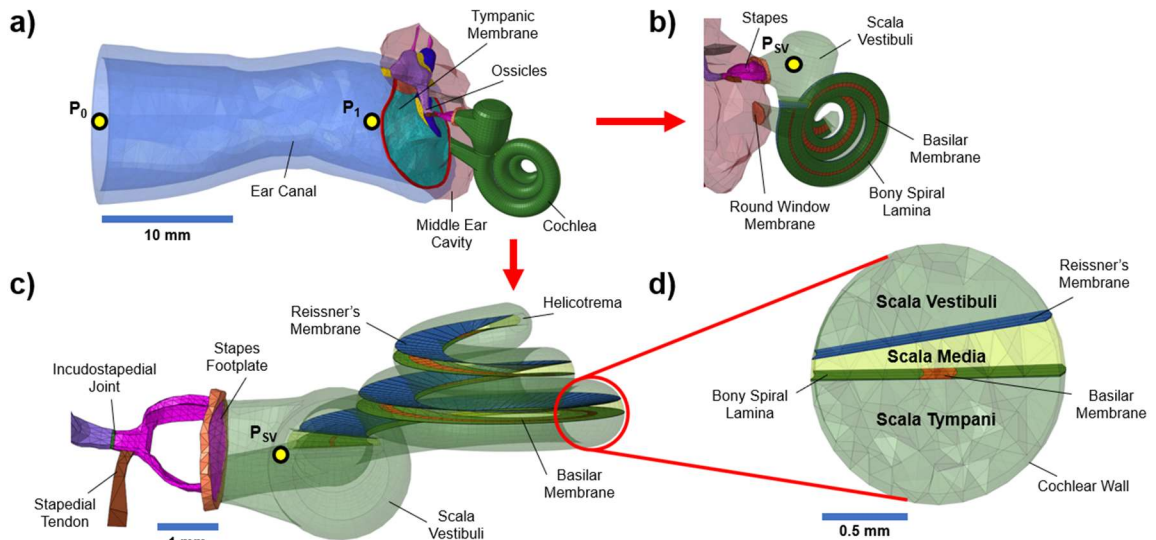
Figure 6. The macroscale FE model of the human ear used in this study. (a) Posterior view of the full 3D FE model, including the ear canal, middle ear, and cochlea. P_0 and P_1 mark the points where input pressure is applied and ear canal pressure is measured, respectively. (b) Magnified view of the cochlea showing the connections between the cochlea and middle ear cavity. P_{SV} reports the SV pressure near the SFP. (c) Superior view of the 3-chambered cochlea showing internal chambers and membranes. (d) Cross-sectional view of the cochlea.

11

2.1.2 Microscale OC Model

The 3D FE microscale model of the OC corresponds to the BM segment located 16.75 mm from the base of the BM. The model, displayed in **Fig. 7(a)**, consists of the BM, TcM, HBs, RL, OHCs, DCs, PhPs, HCs, IPCs, OPCs, IHCs, OSL, and the spiral ligament. The BM has an independent mesh, but is bonded to the OSL, IHC, IPC, OPC, DC, and HC components. The HBs span the TcM and RL, as displayed in **Fig. 7(b)**. Each OHC component is connected to the RL and a DC element, with an associated HB and PhP. Each PhP links a DC to the RL. An individual "row" of the model consists of 3 OHCs arranged in a line, the associated DCs and HBs, and an OPC. The microscale model contains 5 OHC rows, as shown in **Fig. 7(c)**, meaning that there are 15 HBs, 15 OHCs, 15 DCs, 15 PhP, and 5 OPCs. The radial and longitudinal directions used in the OC model are marked in **Fig. 7(c)** as well.
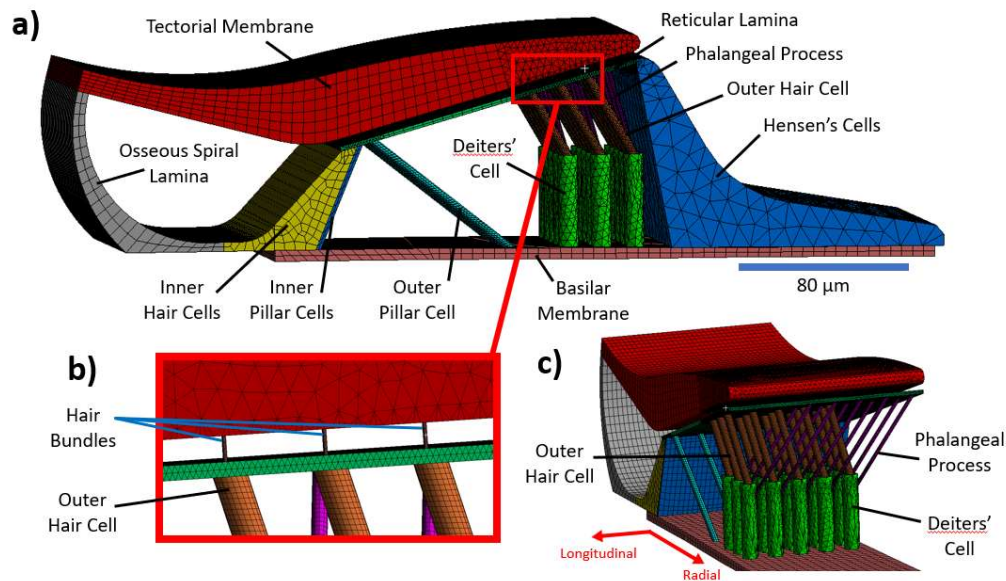
Figure 7. The microscale FE model of the OC. (a) Front view of the OC model, with the membranes, sensory cells, and supporting cells labelled. (b) Magnified view of the HB components connecting the RL and TcM. (c) Side view of the OC model with the HC component hidden, displaying the 5 OHC rows.

The position of the DCs, dimensions of cells and membranes, and sizes of other structures such as the tunnel of Corti (the space between the IPCs and OPCs) were derived from published OC models and histological studies. The dimensions of the model are detailed in **Table 1**. The model's geometry was built in SolidWorks (Dassault Systèmes, Vélizy-Villacoublay, France), and imported into ANSYS Workbench (ANSYS, Inc., Canonsburg, PA). The mesh model was generated using ANSYS Mechanical. The BM mesh does not align with the other model components, so the connection between the BM and the rest of the model is maintained by a mutual bonded contact condition. The OC model contains 32 total components. The components were constructed using linear hexahedral elements, with the exceptions of the DCs, HC, and sections of the RL and TcM in contact with the HBs, which use tetrahedral elements. Using available tools in ANSYS Mechanical, the model was refined to minimize aspect ratio and element count. The structural model consists of 478,676 elements total, due to the mesh refinement needed to connect small components like the HBs with the relatively larger components such as the TcM.

Table 1. The dimensions of the microscale OC model. The table is organized into 3 columns: the structural component of the model and its dimensions, the assigned value of the dimension in the FE model, and the article from which the value was taken.

Structure	FE model	Source
Basilar Membrane (BM)		
Distance from Base (mm)	16.75	Macroscale human ear model
Width	From macroscale model	
Thickness	From macroscale model	
Length	From macroscale model	
Tectorial Membrane (TcM)		
Thickness (μm)	≈ 25	Assumed
Hair Bundle (HB)		
Diameter (μm)	0.4	Zagadou et al. (2014)[27]
Length (μm)	3.5	Wright (1984)[29]
Reticular Lamina (RL)		
Thickness (μm)	0.4	Zagadou et al. (2014)[27]
Angle of RL from BM	15.53°	Meenderink et al. (2019)[30]
Outer Hair Cell (OHC)		
Diameter (μm)	4.5	Assumed
Angle of OHC to DC	30°	Assumed based on Ramamoorthy et al. (2007)[25]
Deiters' Cell (DC)		
Diameter (μm)	9	Assumed
Length (μm)	40	Kolston and Ashmore (1996)[31]
Distance between DCs (μm)	15	Assumed
Location of middle DC	(width of BM)/2	Ramamoorthy et al. (2007)[25]
Phalangeal Process of DC (PhP)		
Diameter (μm)	2	Assumed
PhP span (length) (μm)	34	Assumed, based on Motallebzadeh et al. (2018)[32]
Hensen's Cell (HC)		
Thickness (μm)	10-35	Assumed
Inner Pillar Cell (IPC)		
Diameter (μm)	3.4	Zetes et al. (2012),[33] from image; Zagadou et al. (2014)[27]
Outer Pillar Cell (OPC)		
Diameter (μm)	2	Zetes et al. (2012),[33] from image
Tunnel of Corti (ToC)		
Width (μm)	84.94	Meenderink et al. (2019)[30]
Height (μm)	46.89	Meenderink et al. (2019)[30]
Angle	77.07°	Meenderink et al. (2019)[30]
Inner Hair Cell (IHC)		
Thickness (μm)	6-22	Assumed
Width (μm)	34.49	
Osseous Spiral Lamina (OSL)		
Thickness (μm)	6-22	Assumed
Width (μm)	97.23	Assumed

2.2 Coupled Fluid-Structural Analysis in ANSYS

The macroscale human ear mesh model was imported into ANSYS Workbench. A Fluent/Mechanical coupled fluid-structure-interaction analysis was set up using the System Coupling Service. The Mechanical module simulated the structural components, consisting of the ear canal, middle ear, and cochlear tissues, and the Fluent module modeled the fluid dynamics of the air in the ear canal and middle ear cavity and the fluid inside the cochlea.

2.2.1 Material Properties

The ear canal skin was given material properties identical to those reported in Brown et al.,[20] with a density of 1050 kg/m^3, Young's modulus of 0.42 MPa, and a Poisson's ratio of 0.43. Material properties of the middle ear tissues were derived from experimental studies[34,35] and published FE models[17,22–24,36,37]. **Table 2** details the elastic material properties of the middle ear tissues. The standard linear viscoelastic model in the ANSYS material library was assigned to the TM, IMJ, ISJ, SAL, and RWM with the Prony shear relaxation modulus represented by Eq. [1]:

$$G(t) = G_0 \left[\alpha_\infty^G + \alpha_1^G e^{-t/\tau_i^G} \right] \qquad [\,1\,]$$

where G_0 is the relaxation modulus at $t = 0$, α_∞^G is the relative long-term modulus, α_1^G is the first-order relative modulus, and τ_i^G is the first-order relaxation time. The shear modulus applied to each material was derived from material properties previously published in Zhang and Gan[17] and used in Leckness et al.[24] The Young's Modulus (E) and Poisson's ratio (v) for the material were converted to the shear modulus (G) using Eq. [2]:

$$E = G(1 + v) \qquad [\,2\,]$$

Table 2. The elastic material properties assigned to structures in the middle ear of the macroscale human ear model. All materials had a Poisson's ratio of 0.3.

Structure	FE model	Source
Tympanic Membrane (TM)		
Density (kg/m^3)	1200	Gan et al. (2006)[36]
Young's Modulus (N/m^2)		
Pars tensa	9.5E+7	Zhang and Gan (2013)[17]
Pars flaccida	2.3E+7	Zhang and Gan (2013)[17]
Tympanic annulus	6.0E+7	Zhang and Gan (2013)[17]
Malleus		
Density (avg) (kg/m^3)	3600	Gan et al. (2006)[36]
Young's Modulus (N/m^2)	1.41E+10	Herrman & Liebowitz (1972)[34]
Incus		
Density (avg) (kg/m^3)	3230	Gan et al. (2006)[36]
Young's Modulus (N/m^2)	1.41E+10	Herrman & Liebowitz (1972)[34]
Stapes		
Density (kg/m^3)	2200	Kirikae (1960)[35]
Young's Modulus (N/m^2)	1.41E+10	Gan et al. (2004)[23]
Stapedial Annular Ligament		
Density (kg/m^3)	1200	Gan et al. (2006)[36]
Young's Modulus (N/m^2)	1.28E+7	Zhang and Gan (2013)[17]
Manubrium		
Density (kg/m^3)	1000	Sun et al. (2002)[37]
Young's Modulus (N/m^2)	4.7E+9	Sun et al. (2002)[37]
Incudomalleolar Joint		
Density (kg/m^3)	3200	Sun et al. (2002)[37]
Young's Modulus (N/m^2)	2.4E+8	Zhang and Gan (2013)[17]
Incudostapedial Joint		
Density (kg/m^3)	1200	Sun et al. (2002)[37]
Young's Modulus (N/m^2)	2.04E+7	Zhang and Gan (2013)[17]
Middle Ear Suspensory Ligaments		
C1		
Young's Modulus (N/m^2)	4.9E+6	Gan et al. (2004)[23]
C2		
Young's Modulus (N/m^2)	6.7E+6	Gan et al. (2004)[23]
C3		
Young's Modulus (N/m^2)	6.5E+6	Gan et al. (2004)[23]
C4		
Young's Modulus (N/m^2)	2.1E+7	Gan et al. (2004)[23]
C5		
Young's Modulus (N/m^2)	5.2E+7	Gan et al. (2004)[23]
C7		
Young's Modulus (N/m^2)	7.0E+7	Gan et al. (2004)[23]
Round Window Membrane		
Density (kg/m^3)	1200	Gan et al. (2007)[22]
Young's Modulus (N/m^2)	4.0E+6	Zhang and Gan (2013)[17]

The material properties of the cochlear BM varied along the length of the BM. The mechanical properties of the RM remain understudied[38] but are similar to those of the BM. The cochlear tissue properties are displayed in **Table 3**. The Fluent model had distinct material properties for the fluid components. The ear canal and middle ear air was specified as a compressible, ideal gas with a sea-level ambient pressure (101,325 Pa). The cochlear fluid was assigned an initial density of 998.2 kg/m^3 and viscosity of 1.003×10^{-3} kg/(m·s).

2.2.2 Boundary Conditions

The surfaces of the ear canal skin, TM annulus, suspensory ligaments, stapedial annular ligament, and RWM in contact with the bony wall of the ear were set to fixed boundaries in ANSYS Mechanical simulation. In the cochlea, the supporting bony lamina and the other bones in the cochlea were fully fixed. The edges of the BM and RM in contact with the bony wall were fixed as well. All the walls or solid surfaces contacting the fluid in the Fluent simulation were assigned the no-slip boundary condition.

Table 3. The elastic material properties of the BM and RM in the cochlea. The first and last BM elements are described in order to demonstrate the variation of the BM material properties from the base to the apex of the cochlea.

Structure	FE model	Source
Basilar Membrane		
First Element:		
Width (μm)	130	Gan et al. (2007)[22]
Density (kg/m^3)	1200	Gan et al. (2007)[22]
Young's Modulus (N/m^2)	5.0E+7	Gan et al. (2007)[22]
β Damping Factor	0.0002	
Last Element:		
Width (μm)	500	Gan et al. (2007)[22]
Density (kg/m^3)	1200	Gan et al. (2007)[22]
Young's Modulus (N/m^2)	3.9375E+6	Gan et al. (2007)[22]
β Damping Factor	0.0009685	
Reissner's Membrane		
Density (kg/m^3)	1200	Zhang and Gan (2011)[16]
Young's Modulus (N/m^2)	5.0E+7	Zhang and Gan (2011)[16]
β Damping Factor	0.001	Zhang and Gan (2011)[16]

Fluid-structure interaction (FSI) in ANSYS occurs on defined interface boundary conditions. These interfaces enable communication between the structural and fluid components for FE analysis. In this study, FSI boundary conditions were assigned to the inner wall of the ear canal skin, the ear canal and middle ear facing surfaces of the TM, the SFP surface in contact with the SV, the RWM surfaces in contact with the middle ear and cochlea, the RM surfaces facing the SV and SM, and the BM surfaces facing the SM and ST. With the exception of the RM boundary conditions, these FSI interfaces are identical to those assigned in Brown et al.[21].

2.2.3 System Coupling Analysis, Inputs and Outputs

An experimentally recorded BOP waveform from human TB experiments with a peak pressure of 30.5 kPa (**Fig. 8**) was applied at the entrance of the ear canal as the P_0 shown in **Fig. 6(a)**. The simulation was run for 4 ms, with a time-step size of 1×10^{-3} ms. Both Fluent and Mechanical modules were coupled together using the System Coupling Service to pass structural deformations calculated in Mechanical to Fluent and the fluid force (pressure) calculated in Fluent to Mechanical. Fluid domains were smoothed and re-meshed during the simulation to sustain the mesh quality.

Mechanical outputs from the FE model included all the fluid pressures and structural deformations induced by the BOP or P_0. In this study, the BOP transmission from the ear canal to cochlea was predicted as the ear canal pressure near the TM (P_1) and the intracochlear pressure in SV (P_{SV}) along 5 locations from the base to apex (e.g., 2.5, 5.5, 11.75, 20.5, and 31.75 mm from the base. The model predicted the BOP-induced TM and SFP displacements and the BM movement from the base to apex. In addition, the model predicted the maximum strain and stress distributions of the TM and ISJ.
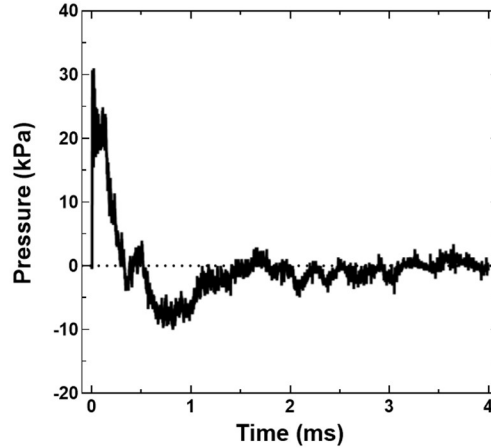
Figure 8. The experimentally recorded BOP waveform applied as input at P0 in the macroscale human ear FE model. The peak pressure is 30.5 kPa.

2.3 Mechanical Analysis of Organ of Corti Model in ANSYS

2.3.1 Material Properties

The components of the OC model were assigned linear elastic material properties, outlined in **Table 4**. The material properties were derived from material tests and other FE models in the published literature. The DC-assigned Young's Modulus was approximated using the elastic rod model in Eq. [3], like the model in Zagadou et al. (2014)[27]:

$$E = \frac{k \times L}{\pi R^2} \qquad [\,3\,]$$

where k is the material stiffness, and L and R are the component length and radius. The Poisson's ratio of all the materials were assumed to be 0.3.

19

Table 4. Linear elastic material properties assigned to structures in the microscale model of the OC. If Poisson's ratio is not listed, it is assumed to be 0.3.

Structure	FE Model Value	Source
Basilar Membrane (BM)		
Density (kg/m^3)	1200	Gan et al. (2007)[22]
Young's Modulus (N/m^2)	1.72×10^7	Gan et al. (2007)[22]
Tectorial Membrane (TcM)		
Density (kg/m^3)	1200	Zwislocki and Cefaratti (1989)[39]
Contacting Hair Cells		
Young's Modulus (N/m^2)	1.10×10^5	Gueta et al. (2006)[40]
Main Body		
Young's Modulus (N/m^2)	3.0×10^4	Gueta et al. (2006)[40]
Hair Bundle (HB)		
Density (kg/m^3)	1200	Assumed
Young's Modulus (N/m^2)	8.6×10^7	Matsui et al. (2006)[41]
Reticular Lamina (RL)		
Density (kg/m^3)	1200	Assumed
Young's Modulus (N/m^2)	1.0×10^5	Motallebzadeh et al. (2018)[32]
Outer Hair Cell (OHC)		
Density (kg/m^3)	1200	Assumed
Young's Modulus (N/m^2)	3700	Sugawara et al. (2002)[42]
Poisson's Ratio	0.82	Spector et al. (1999),[43] isotropic model
Deiters' Cell (DC)		
Density (kg/m^3)	1200	Assumed
Young's Modulus (N/m^2)	6.18×10^6	Elastic rod model, stiffness from Naidu and Mountain (2001)[44]; method from Zagadou et al. (2014)[27]
Poisson's Ratio	0.499	Sugawara et al. (2004)[45]
Phalangeal Process of DC (PhP)		
Density (kg/m^3)	1200	Assumed
Young's Modulus (N/m^2)	4.5×10^7	Laffon and Angelini (1996)[46]
Poisson's Ratio	0.499	Assumed based on Sugawara et al. (2004)[45]
Hensen's Cell (HC)		
Density (kg/m^3)	1200	Assumed
Young's Modulus (N/m^2)	690	Sugawara et al. (2004)[45]
Poisson's Ratio	0.499	Sugawara et al. (2004)[45]
Inner Pillar Cell (IPC)		
Density (kg/m^3)	1200	Assumed
Young's Modulus (N/m^2)	2×10^9	Tolomeo and Holley (1997)[47]
Outer Pillar Cell (OPC)		
Density (kg/m^3)	1200	Assumed
Young's Modulus (N/m^2)	2×10^9	Tolomeo and Holley (1997)[47]
Inner Hair Cell (IHC)		
Density (kg/m^3)	1200	Assumed
Young's Modulus (N/m^2)	290	Sugawara et al. (2004)[45]
Osseous Spiral Lamina		
Density (kg/m^3)	1200	Assumed
Young's Modulus (N/m^2)	8.6×10^7	Matsui et al. (2006)[41]

2.3.2 Boundary Conditions

The input into the model was applied as a displacement boundary condition on the BM face adjacent to the ST. Specifically, the BM displacement was applied on the centerline of the BM, in the location indicated in **Fig. 9**, and applied evenly in the longitudinal direction. This input location is directly underneath the middle DCs. The BM was connected to the OSL, IHC, IPC, OPC, DC, and HC components by a mutual bonded contact connection assigned in ANSYS. The side faces of the BM and walls of the OSL facing away from the OHCs were set as fixed boundaries. Additionally, given the potential for the elements in the TcM and RL to overlap with each other when BM displacement is sufficiently high, a frictionless contact condition was assigned to the TcM and RL walls facing each other to prevent simulation errors.

Given the lack of fluid components in this model, it was not necessary to set FSI interfaces.

2.3.3 Structural Analysis, Inputs and Outputs

The microscale FE model of the OC was simulated using a multi-step static structural analysis in ANSYS Mechanical. The BM displacement 16.75 mm from the base of the BM was reported by the macroscale human ear model. The peak positive and negative displacements in the BM results, representing the BM motion into the SM and ST respectively, were applied to the bottom of the BM as input (**Fig. 9**). The Static Structural module solved each BM displacement case sequentially, in the order they occurred in the transient model.

The model outputs include the deformation of the OHCs, RL, and HBs, as well as the maximum principal strain of the OHCs and HBs. The principal strain measures the

21

strain normal to a body in all 3 dimensions and was selected because of its relevance in predicting tissue injury in other studies. This quantity measured the 3D change in length of the OHC and HB as a preliminary look at potential causes of injury to the OC.

The OHC and HB results were examined for radial and longitudinal variation in the OC behavior. In the radial direction, the OHC and HB positions were labelled as inner, middle, and outer (**Fig. 10**) based on their relative distance from the center of the cochlea's spiral structure.
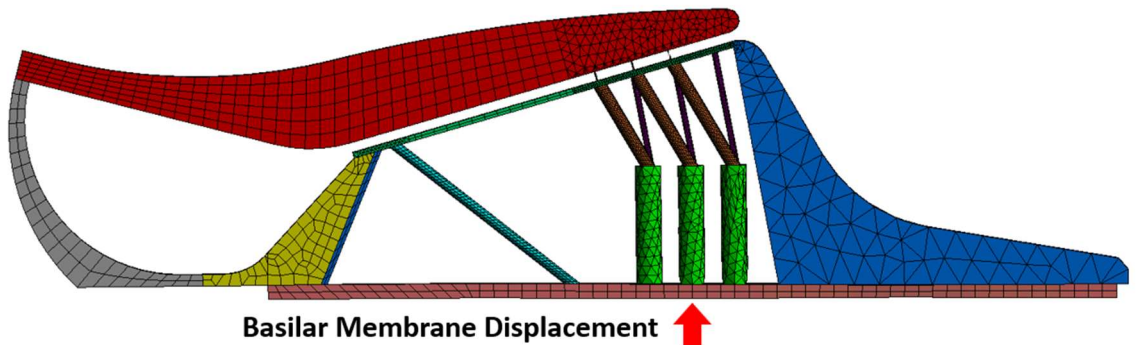
Figure 9. The location where BM displacement was applied as input to the OC model, marked by the red arrow. The BM displacement was applied evenly along the longitudinal direction of the model.
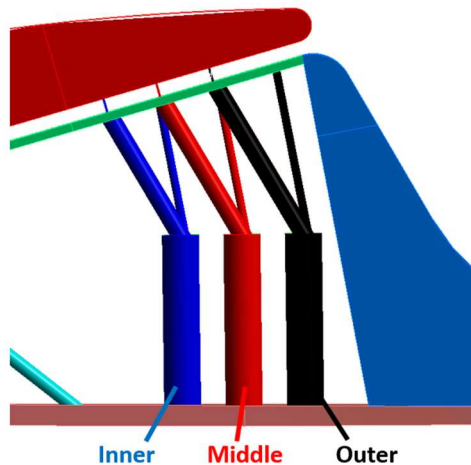
Figure 10. The radial distinctions between OHCs and HBs. The inner, middle, and outer positions are designated by the blue, red, and black colors respectively, based on their distance from the IHCs and the center of the cochlear spiral structure.

2.4 Results and Validation

2.4.1 Experimental Measurement for Validation

The methods used for collecting experimental pressures (e.g., P0 and P1) and movements of the TM and SFP during blast exposure were described in detail by Jiang et al. (2019)[9] and Jiang et al. (2021).[10] Recently, real-time measurements of the SFP motion and intracochlear pressure Psv in human TBs were conducted in our laboratory and reported by Bien et al.[48] Briefly, a pressure sensor (Model 105C002, PCB Piezotronics, Depew, NY) was surgically inserted into the cochlea near the stapes to measure P_{SV} and another pressure sensor (Model 105C02, PCB, Depew, NY) was inserted into the ear canal adjacent to the TM to measure P_1 in a fresh human cadaver TB. The TB was then mounted to a "head block" and placed under the blast apparatus inside an anechoic chamber. The 3rd pressure sensor (Model 102B16, PCB, Depew, NY) was placed at the entrance of the ear canal to monitor P0, the input BOP which was generated by rupturing polycarbonate film(s) (McMaster-Carr, Atlanta, GA) using compressed nitrogen. Two laser Doppler vibrometers (LDVs) were used to measure the movements of the SFP and TB[2]. The LDVs, P_1, and Psv signals were triggered by P_0 and recorded simultaneously.[48] The setup is from Jiang et al. (2021)[10] is shown in **Fig. 11**.
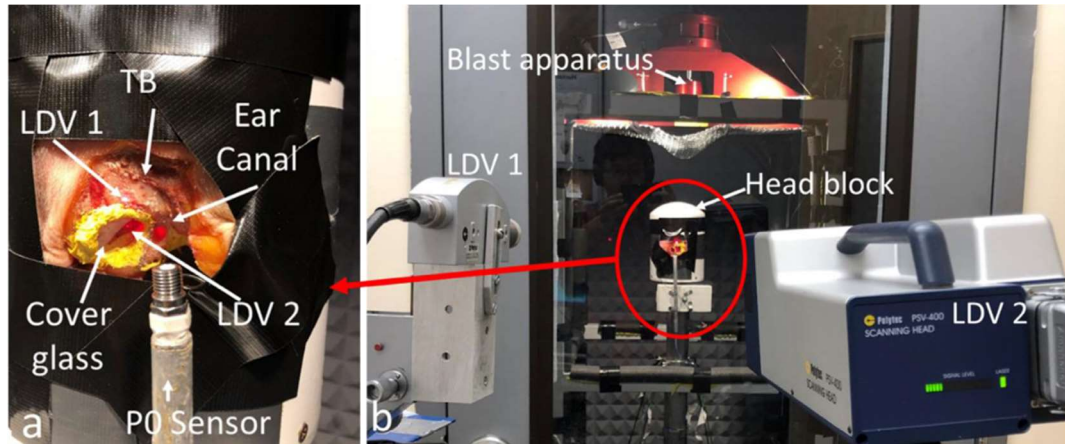
Figure 11. The blast experimental setup used in Jiang et al. (2021). (a) Lasers aim at the TM and SFP of the human TB in the blast apparatus in order to measure their displacements during BOP exposure. (b) The LDVs outside of the blast chamber.

The data acquisition system consisted of a cDAQ 7194, an A/D converter 9215 (National Instruments Inc., Austin, TX), and an oscilloscope (MD04054-6, Tektronix, Beaverton, OR). The P_0, Psv, and LDVs signals were directly acquired using the oscilloscope at a sampling rate of 1 MHz. The P_1 was acquired by a desktop computer using a LabVIEW software package (NI Inc.) at a sampling rate of 100 kHz. All signals were synchronized, and the first positive peak of P_0 was used as the trigger.

The FE model-derived pressure waveforms and displacements of the TM and SFP were compared to the experimental results recorded during blast tests. Three metrics for comparing the P_1 and P_{SV} pressures to experimental results were considered: peak pressure amplitude, ratio over P_0, and waveform A-duration. The peak pressure of P_1 and P_{SV} indicates the intensity of the BOP near the TM and SFP, respectively. The P_1/P_0 ratio represents the ear canal pressure amplification function of the ear canal, and the P_{SV}/P_0 ratio indicates the middle ear pressure amplification function. The A-duration is defined as the time duration of the positive component of the BOP waveform and was determined in this study by taking the time duration (in ms) between the waveform's peak pressure and

24

the end of the initial positive pressure amplitude. The percentage error of these parameters was calculated to quantify the difference between the FE model-derived pressures and experimental values.

The TM and SFP displacements were compared to experimental results using several parameters. The peak TM displacement amplitude into the middle ear and the ratio of the peak-to-peak TM displacement (ΔD) over the P_0 pressure ($\Delta D/P_0$), representing the middle ear transfer function, were used to validate the TM displacement. The peak SFP displacement amplitude into the cochlea and the initial peak-to-peak SFP displacement were used for comparison. Percent error was used to compare the model-derived and experimental values.

2.4.2 Macroscale Human Ear Model Results

The pressures applied at the entrance of the ear canal (P_0) and measured in the ear canal 2 mm away from the TM (P_1) were plotted in **Fig. 12(a)**. The P_1 waveform predicted by the FE model was compared with experimental results in human TBs reported by Jiang et al. (2021)[10] in **Fig. 12(b)**. The P_1/P_0 peak pressure ratios were 2.0 and 1.9 for the modeling and blast test results, respectively, with a percent error of 3.2%. The A-durations of the P_1 waveforms were 0.16 ms and 0.14 ms in the modeling and experimental results, respectively, yielding a higher percent error of 10.7%. Blast-generated air pressure delays with larger distances,[49] explaining the difference in the A-duration.
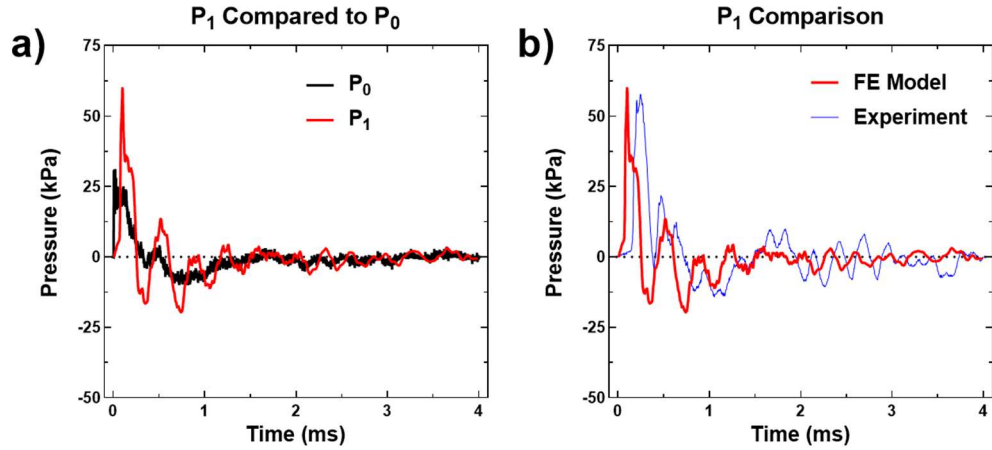
Figure 12. The P_1 pressure near the tympanic membrane in the ear canal predicted by the FE model. (a) The P_0 pressure (black) compared with the model-derived P_1 pressure (red), demonstrating the ear canal amplification. (b) The model-derived P_1 pressure (red) compared to the P_1 pressure resulting from equivalent BOP exposure in Jiang et al. (2021) (blue).

The pressure waveforms in cochlear SV, SM, and ST were plotted in **Figs. 13(a)** to **13(e)**. **Figure 13(f)** shows the locations of the cochlear pressures (CP_1 to CP_5) located 2.5, 5.5, 11.75, 20.5, and 31.75 mm from the base of the BM in all 3 chambers of the cochlea. All pressure signals decreased with time and reached a level below 7 kPa within 4 ms at all locations. The SV and SM pressure curves overlapped with each other at all 5 CPs, with the pressure magnitude in those chambers decreasing from the base to the apex. The ST pressure increased moving from the base to the apex, meaning that the pressure difference across the BM was lower closer to the cochlear apex. Greene et al.[50] reported that for a mean field pressure around the skull of 31.19 kPa, the mean experimentally recorded SV and ST pressures were approximately 18.37 kPa and 17.34 kPa, respectively. This is consistent with the model-derived results from CP_5, which report maximum SV and ST pressures of 19.04 kPa and 19.05 kPa, respectively. The modeling SV and ST pressures have a percent error of 3.65% and 9.86% compared with the experimental results.
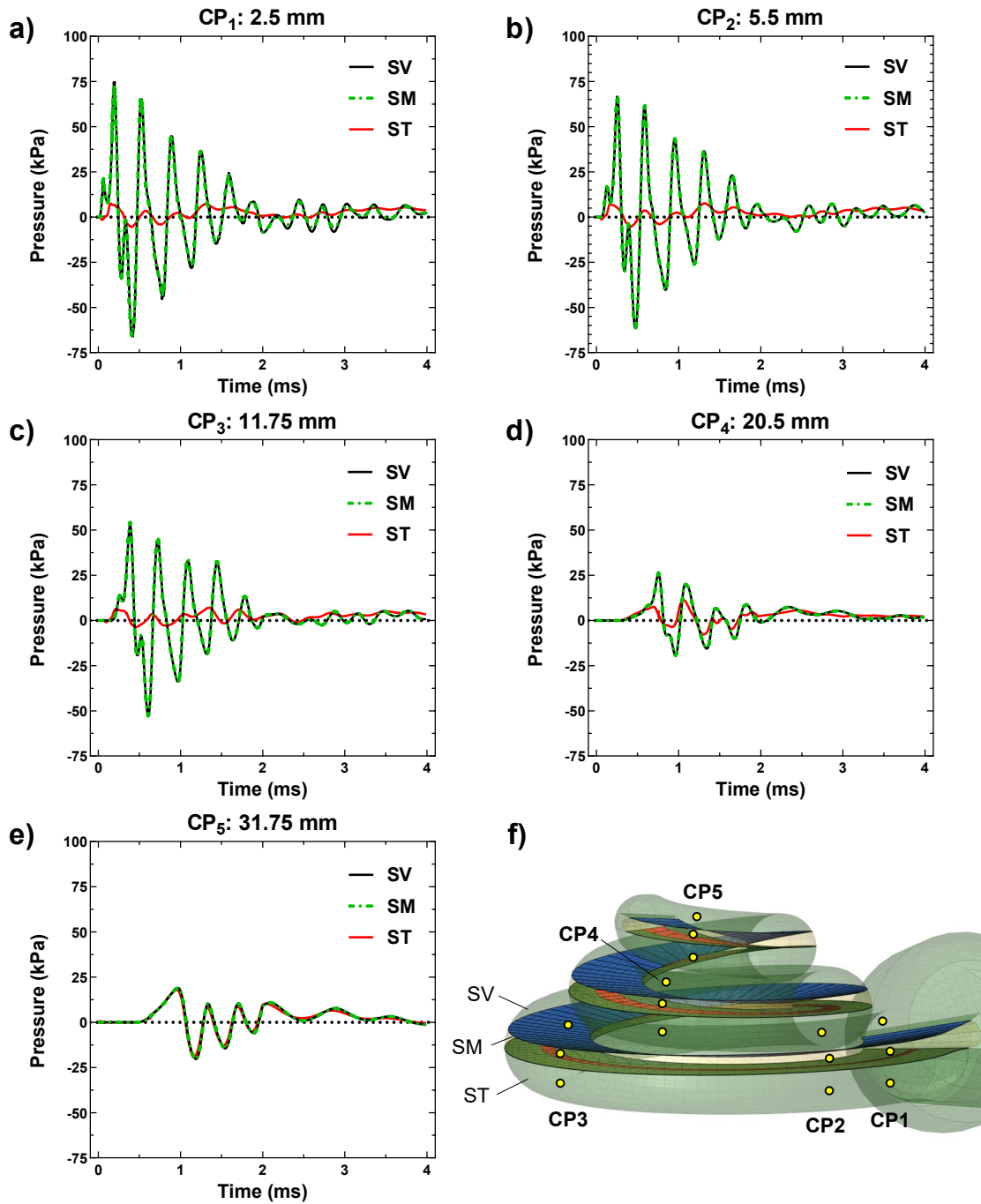
Figure 13. The pressures in the SV, SM, and ST at various points distributed throughout the cochlea. CP_1 (a), CP_2 (b), CP_3 (c), CP_4 (d), and CP_5 (e) are located 2.5, 5.5, 11.75, 20.5, and 31.75 mm from the base of the cochlea, respectively. The SV, SM, and ST pressures are colored black, green, and red, respectively. The locations of all pressure monitor points are shown in (f).

The P_{SV} compared to P_0 in **Fig. 14(a)** was the pressure measured in the SV behind the SFP **(Fig. 6(c))** at the location where intracochlear pressure was measured by Bien et al.[48] The model-derived P_{SV}/P_0 ratio was 4.0, 10.44% higher than the mean of the experimental P_{SV}/P_0, 3.64. The upper and lower bounds of the experimentally measured P_{SV} results under the similar P0 input reported by Bien et al.[48] are shown as a blue shaded region and compared with the modeling values in **Fig. 14(b)**. The magnitudes of the model-derived Psv are within the range established by Bien et al.[48].

The displacement of the TM umbo is shown in **Fig. 15(a)**. Positive TM displacement indicates the membrane is moving into the middle ear cavity. The maximum amplitude of the TM displacement was 321.6 µm at 0.17 ms, corresponding with the maximum P_1 pressure like previous blast models.[20] The SFP displacement obtained from the FE simulation is presented in **Fig. 15(b)**, where the negative displacement indicates movement into the cochlea, and compared to the SFP displacement range published in Jiang et al.[10] in **Fig. 15(c)**. The majority of the SFP displacement reported by the macroscale model was within the range of experimental results. The model-predicted initial peak-to-peak SFP displacement was 67.9 µm. Jiang et al.[10] reported a peak-to-peak SFP displacement of 68.7 µm, giving the modeling results a percent error of 1.19%.
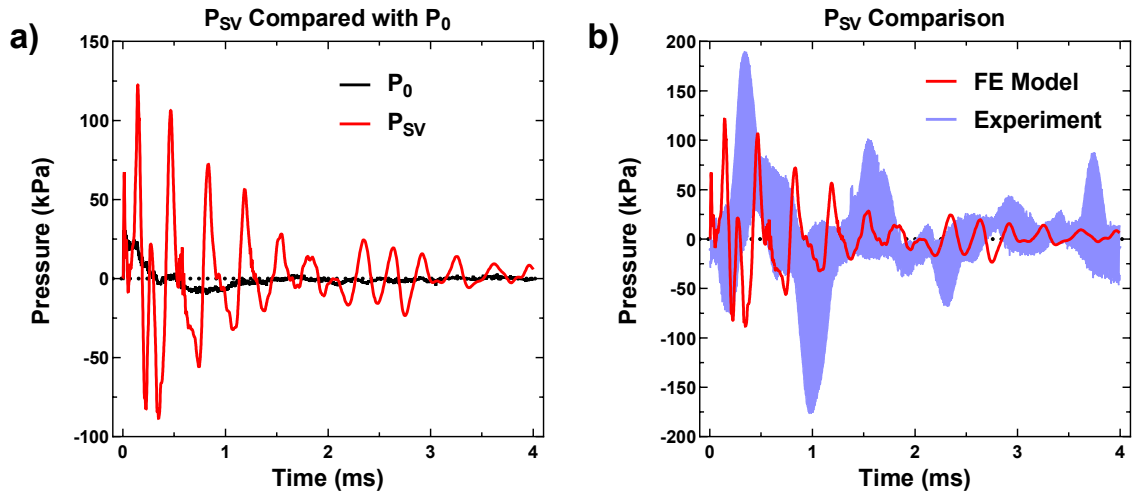
Figure 14. The model-derived P$_{SV}$ pressure near the stapes footplate in the cochlea. (a) The P0 pressure (black) compared with the P$_{SV}$ results (red). (b) The model's P$_{SV}$ pressure compared with the P$_{SV}$ range established by Bien et al. (2022) (shaded blue).
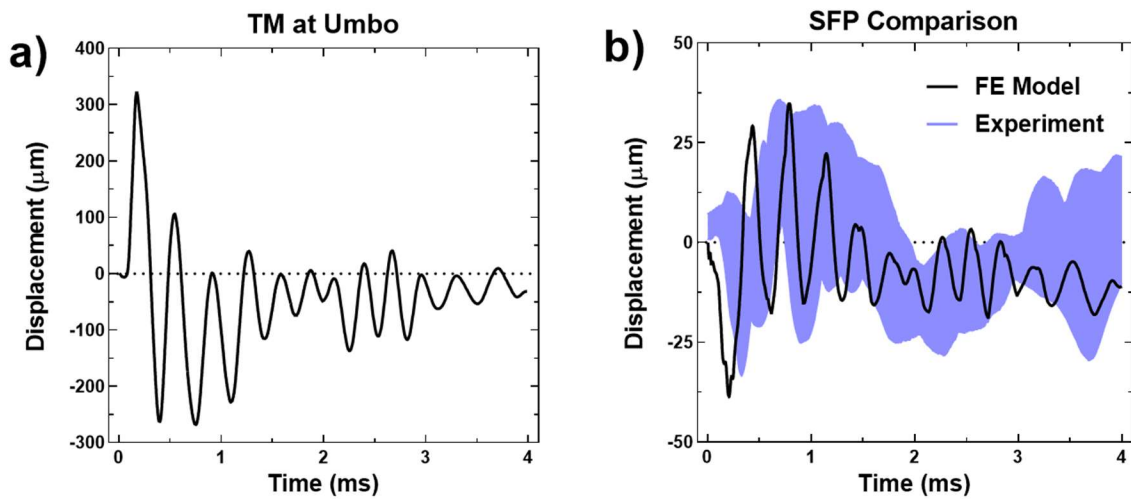
Figure 15. The model-derived displacements of middle ear structures. (a) The model-derived displacement of the TM umbo. Positive displacement indicates movement into the middle ear cavity. (b) The SFP displacement predicted by the model (black) compared with the range of experimentally recorded SFP displacements reported by Jiang et al. (2021) (blue shaded region).

The model-predicted BM displacements are presented in **Fig. 16**. The BM displacements at 4.25, 10.50, 16.75, 23.00, and 29.25 mm from the base of the BM are displayed in **Figs. 16(a-e)**, respectively, with positive displacement indicating movement into the SM. The locations where BM displacement was monitored in the model are shown in **Fig. 16(f)**. The results clearly show the time-dependent transmission of pressure through the cochlea causing BM motion, as the peak BM displacement occurs later moving from the basal to apical BM locations. The predicted peak-to-peak BM displacement was highest in the middle-to-apical region of the BM, consistent with previous blast models.[20,21] Like in Brown et al.,[21] an increasingly negative trend in the BM displacement was observed moving from the base to the apex of the BM. In addition, the initial direction of BM movement was positive at the locations of 10.50, 23.00, 16.75, and 29.25 mm and the amplitude of the first positive peak increased from base to apex.
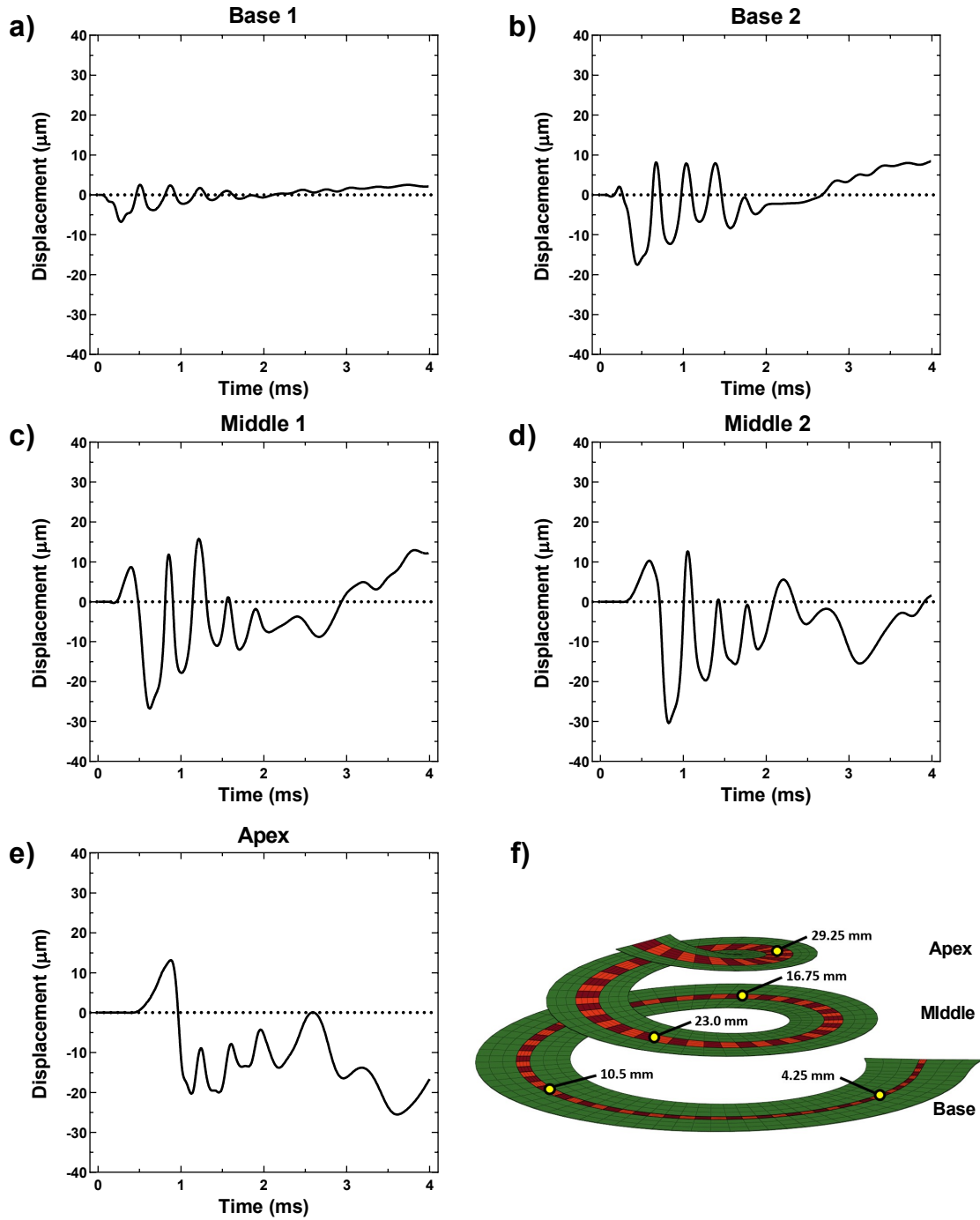
Figure 16. The model-derived displacements of the basilar membrane (BM) at the base, middle, and apex of the cochlea. The displacements at 4.25 mm (a), 10.5 mm (b), 16.75 mm (c), 23.0 mm (d), and 29.25 mm (e) from the base of the BM (positive displacement is into the SV) are displayed, tuned to 11.8 kHz, 5.4 kHz, 2.5 kHz, 1.1 kHz, and 0.5 kHz, respectively. The locations of each BM displacement monitor are shown in (f).

2.4.3 Preliminary Structural OC Model Results

The peak displacements of the macroscale model-predicted BM displacement 16.75 mm from the BM base in the 0 to 2 ms time range were extracted and applied as input to the microscale OC model. The sequential BM displacements for the static structural simulation are shown in **Table 5**. The peak BM displacement into the SM was 15.8 μm, while the peak BM displacement into the ST was 26.8 μm. The significantly higher ST displacement is consistent with the negative displacement trend observed in the macroscale BM displacements (**Fig. 16c**). With these inputs, the model successfully predicted the linear behavior of the OC during blast wave transmission and reported the displacements of the OHCs, RL, and HBs, and the maximum principal strains of the OHCs and HBs. **Figures 17(a)** and **17(b)** show the full OC response at the maximum BM displacements, 15.8 μm and -26.8 μm. As the figures indicate, the region of greatest movement was concentrated around the DCs, OHCs, RL, and the unfixed end of the TcM. The OSL, IHCs and outer region of the HCs showed the least displacement. The RL and TcM also moved much closer to each other during high BM displacement into the SM, but not into the ST.

Table 5. The BM displacement values applied as input to the static structural simulation of the microscale OC model. The displacement at each solution step was taken from the model-derived BM peak results, as shown on the left.
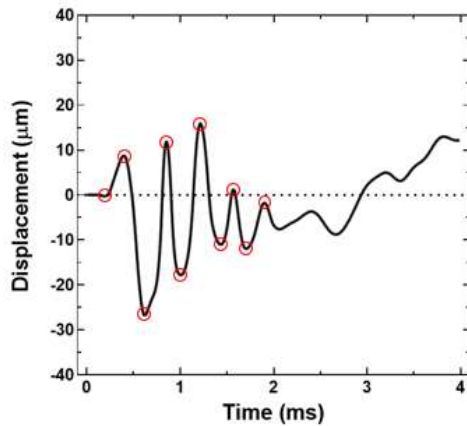
Step	Input BM Displacement (μm)
0	0
1	8.73
2	-26.8
3	11.8
4	-17.8
5	15.8
6	-11.0
7	1.16
8	-11.9
9	-1.85
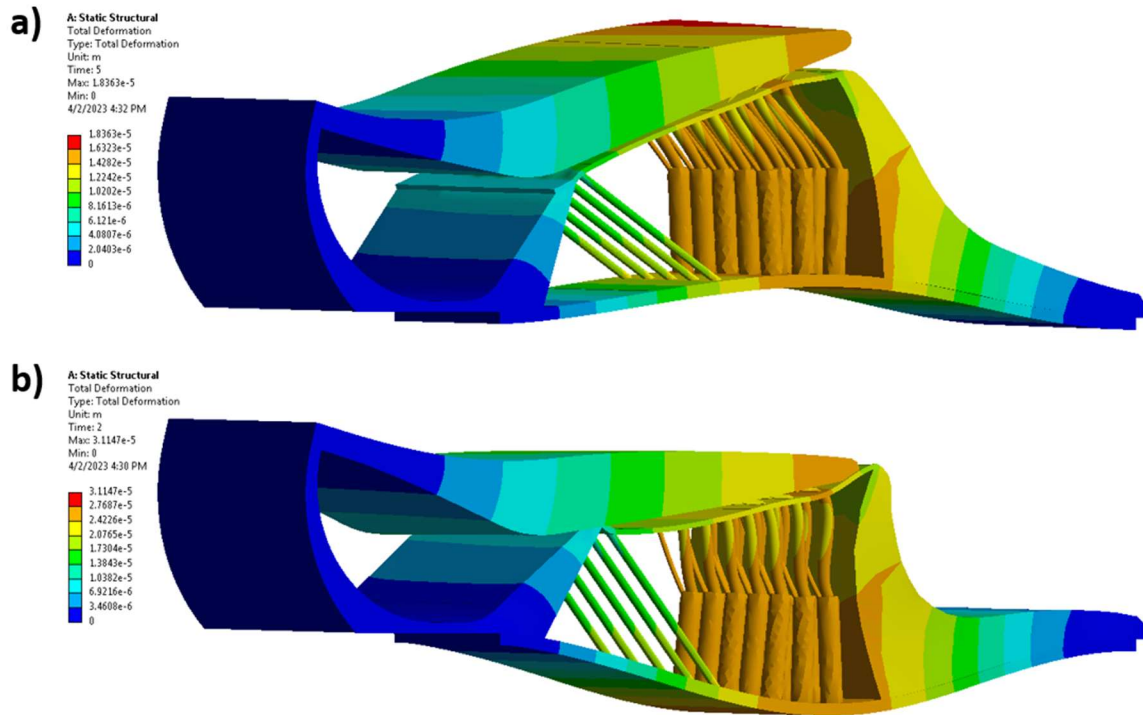
Figure 17. The behavior of the microscale OC model during blast transmission. The OC response during the BM's maximum displacement into the SM and ST are shown in (a) and (b), respectively. As shown by the color bars on the left, blue corresponds to the lowest displacement while orange and red mark the highest displacement.

The displacement of the OHCs versus BM displacement amplitude is shown in **Fig. 18**. **Figure 18(a)** shows the OHC displacement of the inner, middle, and outer OHCs. The OHC displacement displays a linear relationship with the BM displacement. The radial variation in these results is not substantial, with a maximum percent difference of 5.83% when the BM displacement is -26.8 μm. Notably, while the middle and outer OHC displacements align very closely, the inner OHC is more distinct, displaying a slightly lower displacement amplitude than the other OHCs. The longitudinal variation in OHC displacement, illustrated in **Fig. 18(b)**, shows even less of a distinction between the OHC results. This is consistent with other modeling results that indicated longitudinal variation in the model was not significant. The radial variation in the OHC strains is shown in **Fig. 19**. As expected, strain is higher when the BM displacement into the SM or ST is greater.

It is clear based on these results that the middle OHC has significantly less strain than the other OHCs, with a percent difference of 28.02%. This is the first example of the strain results showing greater differences between tissues in the radial direction than the displacement results.

The RL displacements at the maximum BM displacements into the SM and ST are shown in **Figs. 20(a)** and **20(b)**, respectively. The region of the RL connected to the OHC consistently displayed the highest displacement on the membrane, while the areas of the RL connected to the pillar cells and IHCs showed the lowest displacement. Despite the RL region around the OHCs showing the highest displacement, this region never contacted the TcM due to the presence of the HBs.
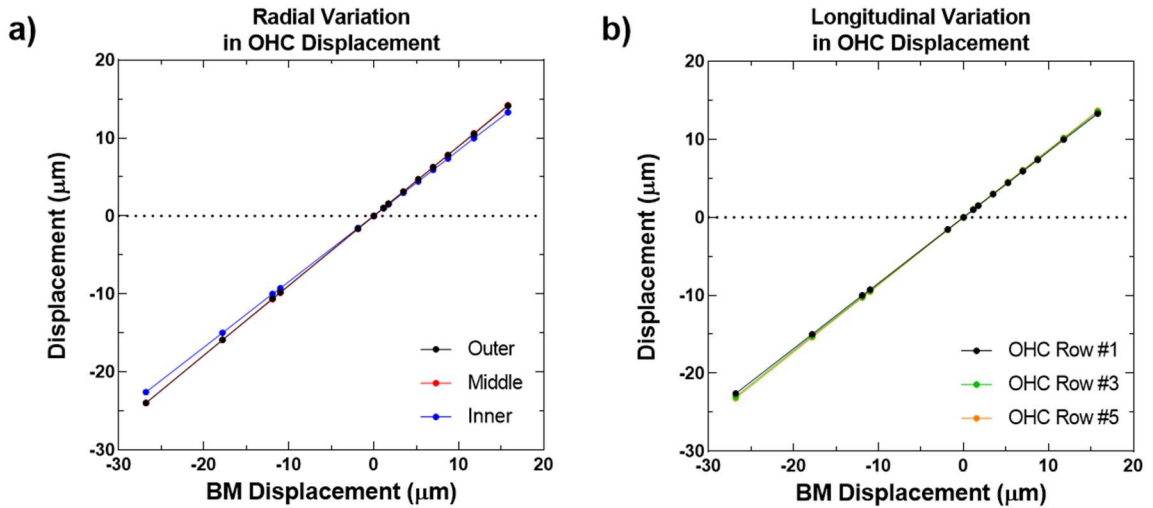
Figure 18. The OHC displacement reported by the microscale model of the OC. (a) The displacement of the outer (black), middle (red), and inner (blue) OHCs, indicating radial variation in the results. (b) The displacement of the 1st (black), 3rd (green), and 5th (orange) rows of OHCs, indicating longitudinal variation in the model. The inner OHC displacement is plotted.
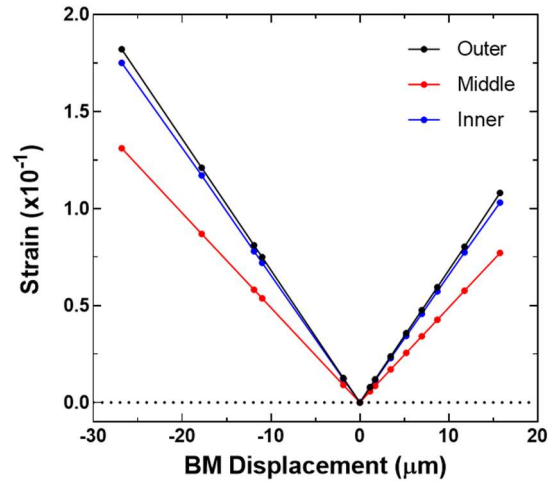
Figure 19. The OHC principal strain reported by the microscale model of the OC. The outer (black), middle (red), and inner (blue) OHC strains are plotted.
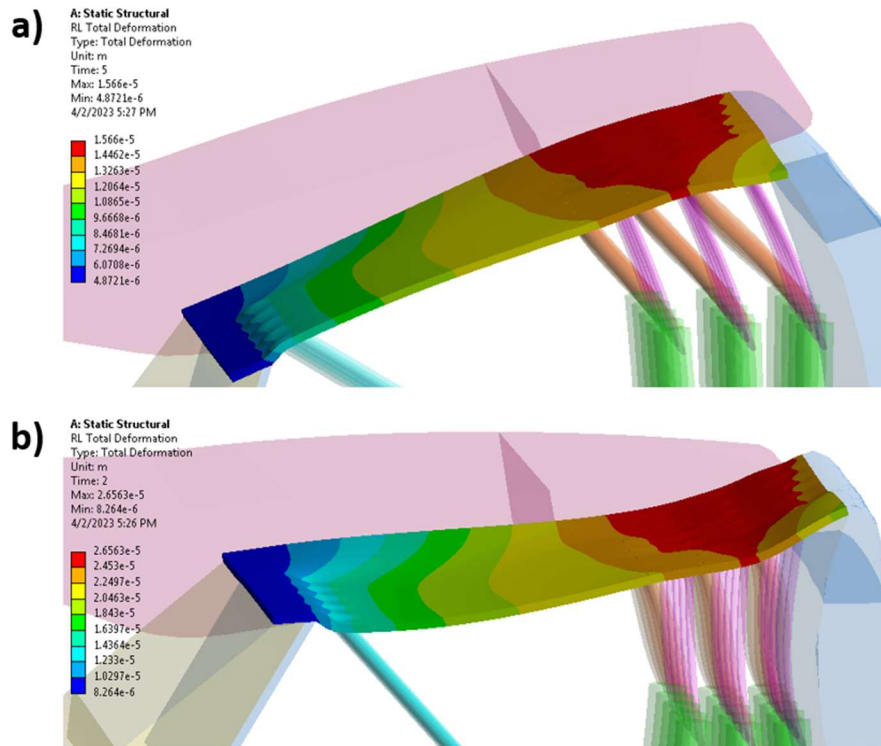
Figure 20. The total RL displacement during blast wave transmission. (a) and (b) show the RL displacement when the BM displacement is 15.8 μm and -26.8 μm, respectively. The left color bars indicate the RL displacement amplitude.

The HBs during the maximum BM displacement into the SM and ST are shown in

Figs. 21(a) and **20(b)**. As **Fig. 21** demonstrates, depending on whether the BM

displacement is into the SM or ST, the HBs will bend inward or outward, respectively. Another pattern is also illustrated by this figure. As BM displacement amplitude increases in either direction, the HBs are moved to be increasingly parallel with the RL. The displacement and strain of the HBs versus the BM displacement is plotted in **Figs. 22(a)** and **22(b)**. Like the OHCs, the HB displacements have a linear relationship with BM displacement. The outer HB displays the strongest displacement amplitude, with the inner HB showing the lowest displacement. The maximum percent difference between the outer and inner HB displacements is 9.96%, greater than the percent difference between the radial OHC displacements. Looking at **Fig. 22(b)**, the middle HB principal strain is significantly lower than the inner and outer HB strains, with a maximum percent difference of 36.27% when the BM displacement into the ST peaks. This is a significant difference, limited only to the middle HB, that does not follow the same pattern as the HB displacement variation.
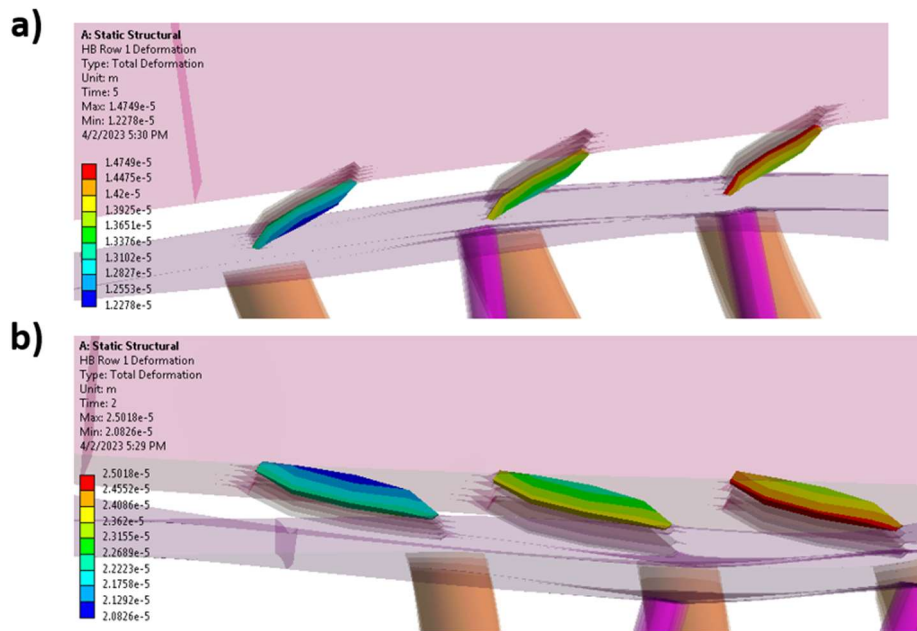
Figure 21. The total HB displacement during blast wave transmission. The HB displacements when the BM displacement is 15.8 μm and -26.8 μm are displayed in (a) and (b), respectively.

36
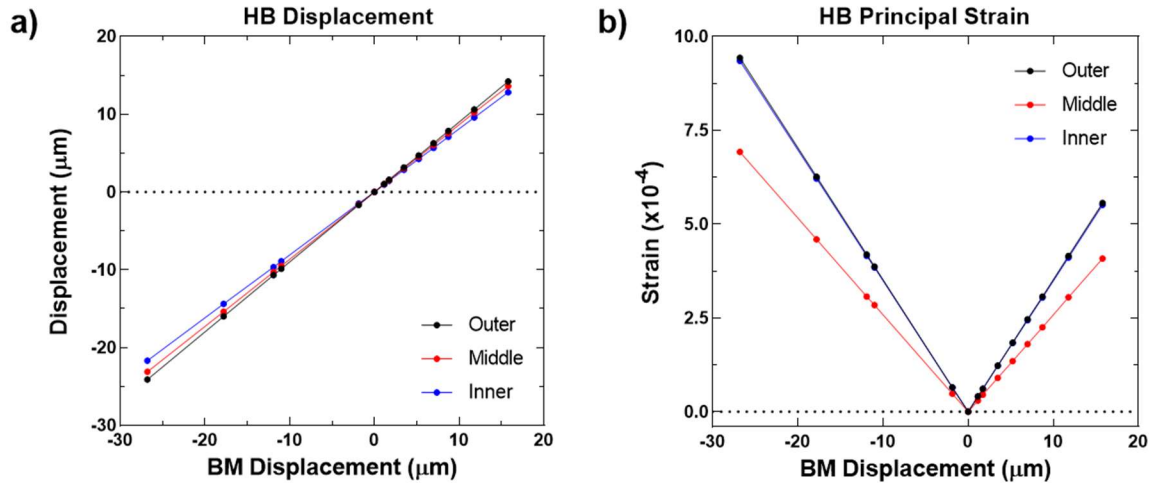
Figure 22. The HB behavior reported by the microscale OC model. The outer (black), middle (red), and inner (blue) HB data is plotted. (a) The HB displacements. (b) The HB strains.

2.5 Discussion

2.5.1 Advancement of Ear Biomechanics with the Spiral Cochlea FE Model

The human ear model described in Chapter 2 was validated by biomechanical measurements of the pressure in the ear canal (P_1), displacements of the TM and SFP, and cochlear pressures (CP_{1-5}, P_{SV}). The pressure amplification of the ear canal, displacements of the middle ear, and pressure transmission through the cochlea were accurately simulated in the model based on comparisons with experimental results. It can be assumed that the development of the 3-chambered spiral cochlea model helped improve the accuracy of the model-derived results.

The influence of the inclusion of the RM and SM in the spiral cochlea on the cochlear biomechanics can be assessed by comparing the results of this model to the 2-chambered spiral cochlea model in Brown et al. (2022),[21] as the same input BOP waveform was used for both studies. Compared to Brown et al. (2022)'s results, the 3-chamber spiral cochlea model reported a higher maximum SFP displacement and decreased cochlear pressures. The SV pressures in Brown et al. (2022) reached up to 175 kPa, more than twice

37

the maximum SV pressure in the 3-chamber model shown in **Fig. 13(a)**. Variation in the BM displacement compared to previous models is also due to the inclusion of the RM and SM. The decreased SV cross-sectional area may be responsible for the drop in pressure between the 2-chamber and 3-chamber cochlea models. For an incompressible fluid, decreasing the cross-sectional area increases the fluid velocity which inversely influences the fluid pressure. When the RM was added to the model, the SV area decreased, increasing the fluid velocity and decreasing the pressure in the SV and throughout the cochlea. This model used a compressible fluid to stabilize the simulation, so the relationship between the change in area and pressure increase is not linear, but it is likely the same principle applies in this case. It is reasonable to conclude that the presence of the RM and SM decreased the pressure in the cochlea by decreasing the cross-sectional area of the SV.

The RM is known to facilitate the transportation of sodium ions between the endolymph (the SM) and the perilymph (the SV and ST),[51,52] have frequency-dependent vibrations in non-human mammals,[53] and potentially play a role in producing otoacoustic emissions.[38] For this biomechanical study, however, the RM appears primarily to passively transmit pressure from the SV to the SM. The results of **Fig. 13** show a constant correlation between the pressure in both chambers (SV and SM), and the RM is a wide, thin, and flexible membrane capable of easily transmitting pressure. The existence of the SM did have a notable influence on BM displacement, allowing for the positive peak to develop moving toward the apex of the BM. The previously mentioned differences between the BM displacement results in the current model and the 2-chambered cochlea model in Brown et al. (2022) were caused by the presence of the SM and the changes in cochlear pressure. The FE model reported in this paper predicted more accurate results than previous models

because of the improvements to its cochlear anatomy, and provided insight into the influence of the RM and SM on cochlear biomechanics.

2.5.2 Contribution of the OC model to multiscale modeling of the auditory system

In addition to the improved anatomy of the cochlea in the macroscale model, the most significant advancement of blast wave transmission FE models described in this chapter is the integration of the microscale model of the OC. Previous studies have modeled the inner ear during blast wave transmission[20,21] or integrated an OC model with a macroscale cochlea model,[26,28] but the integration of the microscale OC model with a macroscale model of the full human ear, used for a high deformation blast transmission analysis, is completely novel. The OC model was able to simulate the motion of the OHCs, RL, and HBs during blast transmission in a linear analysis, offering new insight into the behavior of the OC during blast wave transmission. This is a crucial step towards developing a more advanced multiscale model of the human ear that uses the macroscale cochlea's BM displacements as input into the OC model.

Unfortunately, due to a lack of experimental data measuring the motion of OC tissues during BOP exposure and the limited nature of the structural analysis conducted in this study, the OC model's preliminary results could not be verified. However, the predicted OHC and HB displacements and strains do have interesting implications for OC mechanics. The results do indicate a certain degree of radial variation in OHC and HB behavior, more pronounced in the HBs and in the strain results. Additionally, the differences were more significant when the BM displacement amplitude was greater. This indicates that the likelihood of injury to the somatosensory OHCs and HBs could vary depending on their position within the OC.

It has been documented that inner ear injury caused by blast exposure is distinct from injury occurring due to prolonged noise exposure. While prolonged high noise exposure can lead to OHC death and the disappearance of stereociliary bundles, blast exposure typically results in the disruption of stereociliary bundles, typically the outer layer of stereocilia.[54] Scanning electron microscope images of blast-exposed chinchilla ears, such as the image in **Fig. 23**, show the outer stereocilia, which connect to the TcM, "splayed out".[54] The FE model-predicted HB motion (**Fig. 21**) showed significant movement, with the HBs pushed against the RL. The preliminary results describing HB motion in the OC model may hint at the process by which the stereocilia connected to both the RL and TcM become disrupted and splayed out.
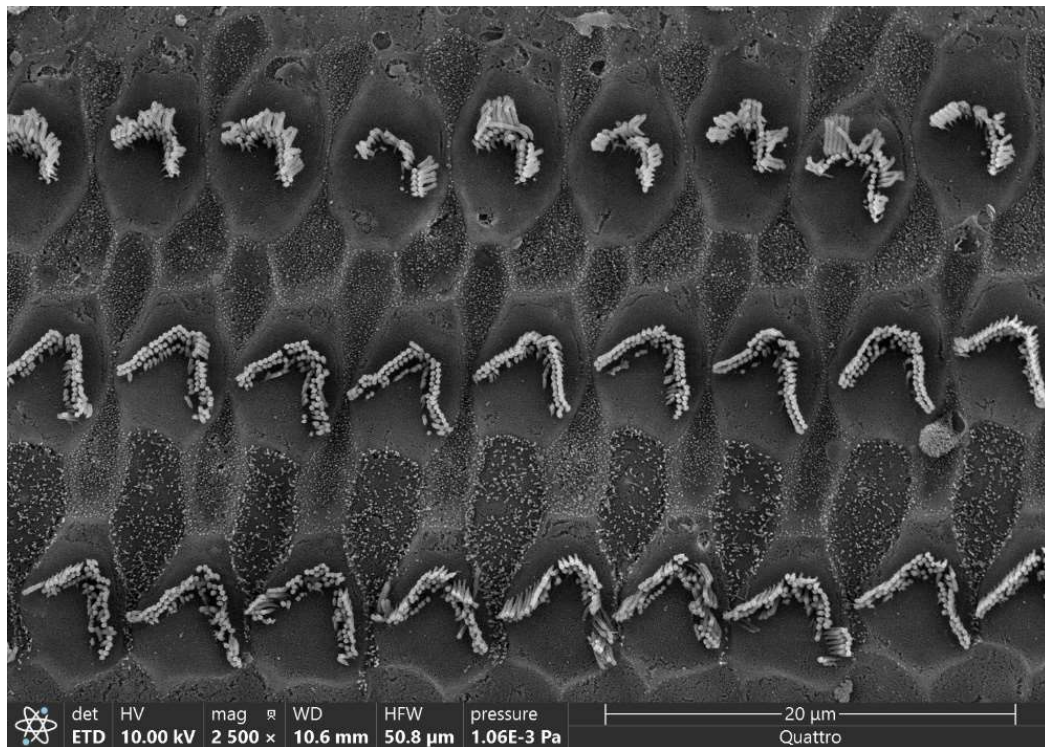
Figure 23. Scanning electron microscope image of the stereocilia on the middle turn of the BM in the cochlea of a blast-exposed chinchilla's left ear. The top row of HBs show the outer row of stereocilia splayed out.

2.6.3 Limitations and Future Study

The multi-layered, fiber-embedded microstructure of the TM will be incorporated in future updates of the macroscale model to investigate the mechanism and impact of the blast-induced structural damage to the TM.[55] The complicated microstructure of the BM willals o be considered in the future development of this model. The human BM is a multi-layered, non-isotropic membrane embedded with radial collagen fibers with thickness varied in the radial direction.[56] The isotropic BM yielded much slower high-frequency roll off, which should be improved by considering the orthotropic microstructure of the BM.[57] Notably, the predicted BM displacement of the model has not been experimentally validated due to a lack of published experimental results. The development of a novel experimental setup to measure the motion of the BM during blast exposure would allow the accuracy of the modeling results to be confirmed.

In this study, only a single BOP waveform was applied as input to the model. Future modeling studies will apply multiple waveforms over time to simulate repeated blast exposure. This will enable a closer study of the mechanisms contributing to temporary threshold shifts due to blast exposure and permanent threshold shifts caused by multiple blasts.

The preliminary FE analysis performed using the microscale model of the OC was very basic. Future studies need to account for the viscoelastic properties of the TcM and BM,[26] as well as other OC tissues. A time-domain analysis, using the full BM displacement reported by the macroscale model, must be conducted to better understand the behavior of the OC during blast. This will require more work on the structure and mesh of the model to avoid element distortion in a high deformation, transient analysis.

The focus of the OC modeling study in this thesis was on the OHC behavior during blast wave transmission. Relative to the OHCs, the IHCs were neglected, as their behavior was not reported and they were represented as a single component. Due to the high displacement of the BM in the center of the membrane, where the OHCs are located, the OHCs are more strongly affected by blast exposure than the IHCs. In addition, the DPOAE signals measured following blast tests are a measure of OHC function, allowing for comparison between the experimental and modeling results. However, future studies may represent the IHCs as individual cells. Additionally, OC models 4.25 mm and 28.25 mm from the base of the BM will be developed in order to understand how the OC response to blast wave transmission varies along the length of the cochlea.

Chapter 3: Applications of the Human Ear Model

The FE model of the human ear was developed to simulate blast wave transmission from the external ear canal to the cochlea and predict the behavior of the OC and hair cells within the cochlea. The results of the model and the mesh model itself can be applied to multiple different studies, such as predicting the likelihood of hearing loss and evaluating the performance of HPDs.

3.1 Auditory Injury Prediction

The likelihood of injury occurring in the middle or inner ear due to BOP exposure can be predicted using several established metrics. Published literature has established thresholds for TM strain,[58,59] incudostapedial joint (ISJ) strain,[60,61] TM displacement,[9] and SFP displacement[10] during blast wave transmission where injury to the middle ear tissue becomes likely. The military standard for predicting high-intensity noise and blast-induced hearing loss is the Auditory Hazard Assessment Algorithm for Humans (AHAAH). The AHAAH model relates hearing loss caused by noise and blast exposure in animal experiments to results in numerical animal models, and converts that data to human models.[62,63] AHAAH is a one-dimensional lumped model, and expresses the likelihood of auditory injury is expressed as auditory risk units (ARUs)[64]. The model has been validated against military clinical studies[62,64] and is a simple tool for end-users. Zagadou et al. (2016)[65] proposed an expansion of the AHAAH model that predicts energy entering the cochlea as an indicator of likely hearing loss. Cochlear energy flux has been calculated using experimental results in some blast studies.[48] The methods for predicting these injury indicators are compatible with the results that can be derived from FE mechanical models of the ear.

3.1.1 Strain Threshold Analysis

Published experimental and modeling studies have investigated the conditions necessary to rupture, tear, or otherwise injure tissues in the middle ear. The strains necessary to damage the TM and ISJ have been published in several papers. Because the FE model of the human ear predicts the strains of all structural components at all time points, the strains calculated by the model can be compared to strain thresholds in the literature.

The distributions of the strain and stress within the TM at the time when the maximum strain or stress appeared were plotted in **Figs. 24(a)** and **24(b)**, respectively. The maximum principal elastic strain reported on the TM was 0.23 at 0.15 ms, concentrated on the TM annulus approximately 3 mm inferior and anterior to the TM umbo. The maximum principal stress reached 14.2 MPa at 0.16 ms, concentrated on the TM umbo. Cheng et al.[58] reported the strain threshold for TM injury as approximately 0.23 ± 0.06. The TM strain reported for this model does not surpass this threshold, but a higher pressure BOP likely would, causing TM injury or rupture.

Figures 25(a) and **25(b)** show the maximum distributions of stress and strain on the ISJ. The maximum principal elastic strain reported on the ISJ was 0.75 at 0.76 ms, and the maximum stress was 9.1 MPa at 0.39 ms. The ISJ reported a greater principal strain but lower stress than the TM. The static ISJ failure strain was determined by Zhang and Gan to be 1.04 ± 0.12.[60] The ISJ strain reported by the macroscale model does not surpass this threshold, so using this standard, it would be predicted that the ISJ would not be injured to the exposure to a 30.5 kPa BOP. An alternate high strain rate failure threshold is

approximately 0.1, as established by Jiang[61]; using this criterion, the ISJ would be at risk

of failure, and could contribute to the disruption of the ossicular chain.
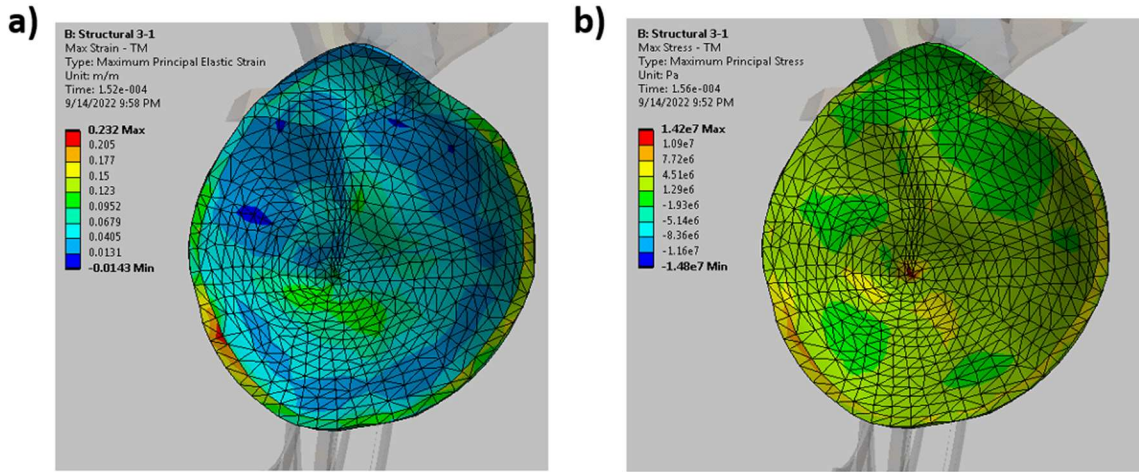
Figure 24. The strain and stress on the TM surface predicted by the model and used to predict the likelihood of TM rupture. (a) Maximum principal strain distribution on the TM surface. (b) Maximum stress distribution on the TM.
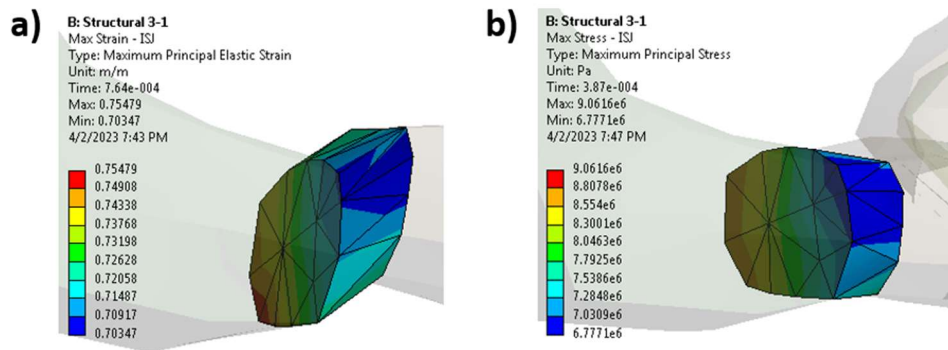
Figure 25. The strain and stress on the ISJ predicted by the model and used to predict the likelihood of ISJ injury. (a) Maximum principal strain distribution on the ISJ. (b) Maximum stress distribution on the ISJ.

3.1.2 Auditory Risk Units

ARUs indicate the likelihood of auditory injury resulting from noise or blast exposure as predicted by the AHAAH model. AHAAH is a lumped-element model, but ARUs can be predicted using FE modeling as well. ARUs are calculated using Eq. [4]:

$$ARU = \sum (d_{BM})^2 \qquad [\,4\,]$$

where d_{BM} is the displacement of the BM at a specific point on the membrane.

For the purposes of this study, ARUs were calculated at 23 locations along the length of the BM. The summation was carried out for 2 ms of data immediately following the BOP peak pressure, with the data normalized by time step size. The ARUs corresponding to the model-derived BM displacements are shown in **Fig. 26**. The maximum calculated ARU value is approximately 69,000, occurring 25.5 mm from the base of the BM. The highest ARUs are concentrated around the middle to apical region of the BM. This is consistent with the results reported in Brown et al. (2021).[20] Based on this analysis, it would be expected that blast-induced injury would be more common in the middle to apical region of the cochlea within the inner ear.
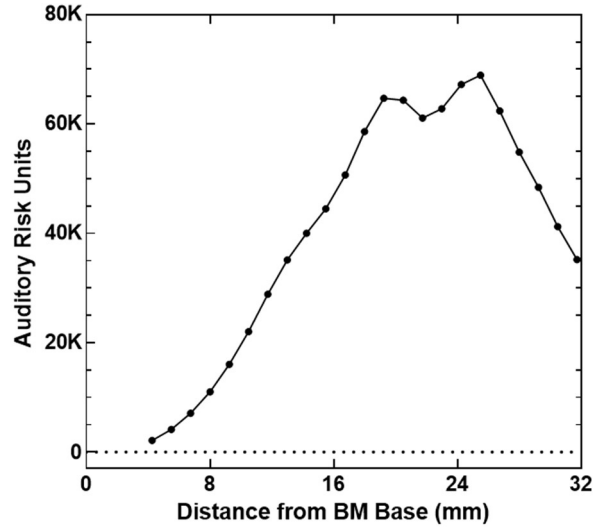
Figure 26. Auditory risk units calculated based on the BM displacements predicted by the macroscale human ear model. The highest ARU values are concentrated in the middle to apical region of the BM.

3.1.3 Energy Entering Cochlea

The energy entering the cochlea has been proposed as a potential indicator of cochlear injury after blast exposure.[65] The energy entering the cochlea as a function of time was determined based on the reported velocity of the SFP and the pressure in the SV near the SFP. The flux of energy entering the cochlea was calculated with the following Eq. [5][65]:

$$E^* = |P_V(t)V_S(t)| \qquad [\,5\,]$$

where P_V(t) was the SV pressure and V_S(t) was the SFP velocity.

The total energy entering the cochlea can be calculated using the energy flux as explained by Eq. [6]:

$$E = \int_0^T E^*A \, dt \qquad [\,6\,]$$

where A was the surface area of the SFP, t was the time, and T was the duration of time elapsed.

Cochlear energy was calculated using both the results from the FE model and experimental measurements from blast tests.[48] The SFP velocity calculated from the SFP displacement data and the P_{SV} pressure were used to calculate the energy entering the cochlea in **Fig. 27**. **Figure 27(a)** displays the calculated energy flux at the SFP in the cochlea. The highest energy flux, 67 kJ/(m^2*s), occurred at 0.34 ms, roughly corresponding to the point in time where the SFP had the highest velocity, moving back from the SV towards the middle ear cavity. The second-highest flux, 61 kJ/(m^2*s), occurred at 0.14 ms, while the stapes footplate was pushing into the SV, and was close to the P_{SV} peak. These points in time corresponded with the sharpest increases in energy entering the cochlea. The total energy entering the cochlea is illustrated by **Fig. 27(b)**. During the 4 ms of blast transmission simulated in the macroscale ear model, 77.7 µJ of energy entered the cochlea via the movement of the SFP.

Bien et al.[48] calculated the energy entering the cochlea based on experimental measurements of the SFP velocity and intracochlear pressure. Some of their reported experimental results induced a similar maximum energy flux, but unlike the modeling results, their results had one prominent peak instead of several intense peaks of short duration. This is attributable to the high fluctuations of the P_{SV} pressure in the FE model. The total energy entering the cochlea over 4 ms following the blast was 61.9 µJ in the experimental results. This yields a percent error of 25.6% between the experimental and modeling cochlear energies. With more experimental results or changes to the model's vestibular structure near the SFP, the model might be demonstrated to accurately predict the energy entering the cochlea following blast exposure.
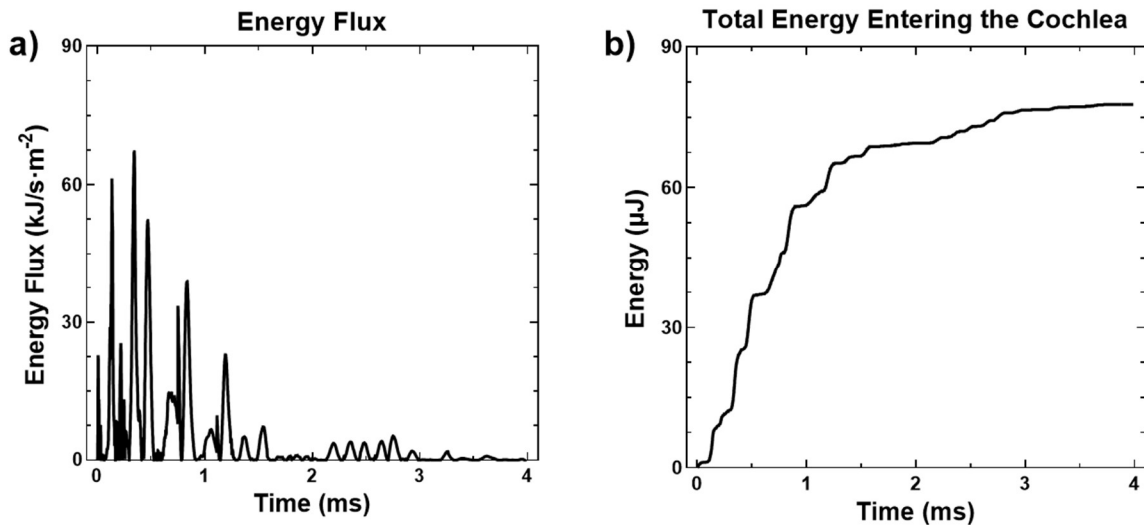
Figure 27. The total energy entering the cochlea over time calculated based on model-derived outputs. (a) The energy flux entering the cochlea is calculated as a function of the predicted SFP velocity and PSV pressure. (b) Total energy entering the cochlea over time, calculated as the integral of energy flux and SFP area over the 4 ms time domain.

3.2 Earplugs & the Occlusion Effect

Previous blast models of the ear have been used to simulate the effect of earplugs on blast attenuation.[66] In this way, the blast transmission FE model can be used to evaluate the effectiveness of earplugs in preventing blast-induced auditory injury. However, this method of simulating earplugs neglects the phenomenon known as the occlusion effect (OE). The OE is the amplification of low-frequency sound transmitted through the ear canal walls via bone conduction (BC) when the canal is occluded by objects like earplugs or other HPDs. BC sound is caused by the vibration of the temporal bone induced by atmospheric vibrations. When the temporal bone vibrates adjacent to the air in the ear canal, the air is compressed and expanded, generating a sound in the ear canal.[67] The outer-ear pathway for BC hearing is negligible in an open ear canal, but in an occluded ear canal, BC sound eclipses air-conducted sound below 1 kHz,[67] forming the basis of the OE.[68,69]

HPDs are used to protect service members from noise-induced hearing loss and tinnitus, the most common disabilities diagnosed in military servicemembers and veterans.[6,70] However, studies indicate that earplug use among active military servicemembers is very low.[71,72] The low compliance in HPD use contributes to the high occurrence of hearing loss and tinnitus due to unprotected noise exposure among veterans.[73,74] Discomfort caused by the OE may account in part for low HPD use; as such, it is important to investigate and understand this phenomenon. It is a novel effort to model the OE using this blast model.

3.2.1 Finite Element Modeling

Two new meshes for the earplugs and adjusted ear canal air were generated for this analysis. Three earplugs were examined during the study, shown in Fig. 2. A full earplug mesh was created based on the geometry of standard foam earplugs (**Fig. 28(a)**), consisting of 711 elements. This mesh was also used on the earplug made of an experimental nanoporous aerogel (NA) material designed by Dr. Hongbing Lu's lab (**Fig. 28(c)**). To partially simulate the poroelastic behavior of the NA material, it was assigned material behavior using the Prony Shear Relaxation model described in Eq. [1]. This earplug fully occludes the ear canal entrance. An alternate earplug FE geometry based on silicone combat arms (CA) earplugs (**Fig. 28(b)**) was constructed out of 23,440 mesh elements. A cylindrical orifice of 2 mm in diameter runs through the earplug, and the earplug separates two EC air domains from the rest of the EC cavity. The earplug material properties are displayed in **Table 6**. The adjusted ear canal mesh was connected with the macroscale model's middle ear and cochlea, displayed in **Fig. 6**.
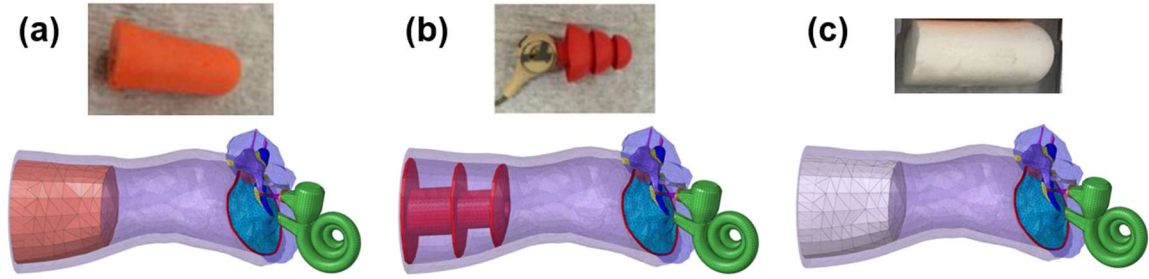
Figure 28. The earplugs tested during the OE modeling study. The physical earplug and FE model of the classic foam earplug (a), CA earplug (b), and NA earplug (c) are displayed.

Table 6. The material properties assigned to the earplug components.

Structure	FE Model
Foam	
Density (kg/m^3)	230
Young's Modulus (N/m^2)	2.2×10^4
Poisson's Ratio	0.1
Silicone	
Density (kg/m^3)	1150
Young's Modulus (N/m^2)	1.5×10^6
Poisson's Ratio	0.48
Aerogel	
Density (kg/m^3)	370
Young's Modulus (N/m^2)	2.65×10^5
Poisson's Ratio	0.48

These models were imported into the ANSYS Workbench environment for analysis. Two separate simulations were set up for each earplug. A coupled acoustic-structural simulation was created using ANSYS Mechanical to examine the response of the ear over a frequency range of 100 to 10000 Hz. 90 dB was applied uniformly on the ear canal entrance (P_0). The EC, middle ear cavity and cochlear bony walls were set to impedance boundaries with a resistance of 1.5×10^5. The walls of the TM in the EC and middle ear, the OWM and RWM, the BM in the cochlea, and any earplug walls facing into the EC were all set to behave as FSIs. The P_1 pressure was tracked in order to assess the influence of the OE.

BC stimulation was applied directly to the EC walls due to the lack of simulated tissues surrounding the EC in this model and for simplicity. A normal volume velocity was applied to the EC walls in simulations with BC stimulation. The amplitude of this velocity is 10^{-5} m/s, the same value used in Carillo et al.,[69] though this model's EC wall stimulation is simpler and does not account for velocity distribution along the wall. **Fig. 29** shows the amplitude and location of the BC stimulation used during simulation. Simulations with and without BC stimulation were run.
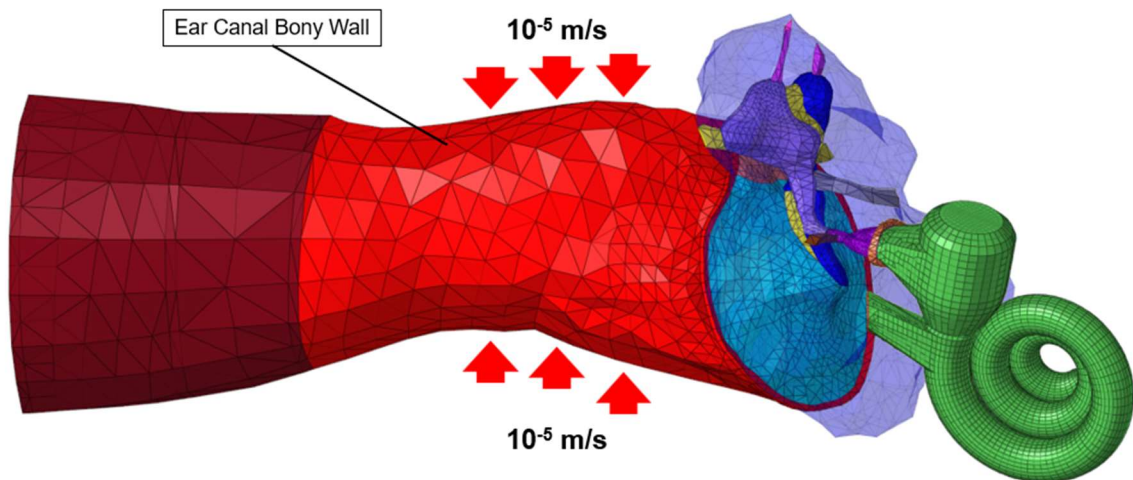
Figure 29. FE model of the human ear with a velocity boundary condition of 10^{-5} m/s applied normal to the bony ear canal wall to simulate BC hearing.

3.2.2 Results & Discussion

Figure 30 displays the calculated P1 pressure from the acoustic simulations. **Fig. 30(a)** shows the P_1 pressure when 90 dB is applied external to the EC entrance, with no BC stimulation at all. As illustrated, open ear pressure stays relatively steady at 0.64 Pa below 1 kHz. The open ear P_1 pressure shows two peaks, at 3 and 9 kHz. The P_1 pressure with a foam earplug present has two peaks, at 0.17 and 0.5 kHz, where its pressure is greater than the open ear simulation. The CA plug shows a single peak at 0.8 kHz where it surpasses the open ear pressure. Finally, the NA earplug prevents the P_1 pressure from being greater than P_1 in the open ear but has relative peaks at 0.15 and 0.6 kHz. All earplugs caused a decrease in pressure after 1 kHz, ending in a relative peak between 9 and 10 kHz.

The addition of BC stimulation, produced by the normal 10^{-5} m/s velocity field on the EC wall, produced the P_1 pressure results shown in **Fig. 30(b)**. The open ear P_1 pressure is negligibly affected by BC stimulation, and the CA P_1 pressure is only minimally increased by BC stimulation. All earplugs induce a P_1 pressure peak greater that the open ear canal pressure when below 1 kHz. The foam earplug shows peaks at 0.17 and 0.5 kHz, reaching 10.25 Pa and 3.56 Pa, respectively. The CA plug retains its peak at 0.8 kHz of approximately 9.47 Pa. Unlike the results in **Fig. 29(a)**, with BC stimulation the aerogel earplug displays a major peak at 0.5 kHz of 6.74 Pa, respectively. After 1 kHz, the earplug-affected results show a gradual decrease in pressure like in the results without BC stimulation.
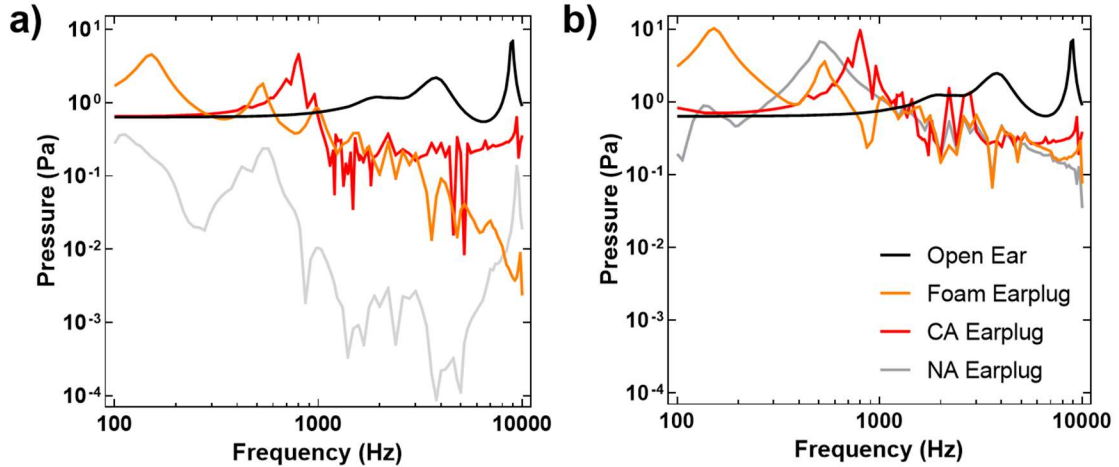
Figure 30. The FE model's predicted P_1 pressure from the harmonic acoustic analysis for the open ear, foam, CA, and experimental NA earplugs. The P_1 pressure when 90 dB of acoustic pressure is applied outside of the ear canal is without (a) and with (b) BC stimulation is presented.

Fig. 31 displays the SFP displacement amplitude in nanometers (nm) in the acoustic simulations with (**Fig. 31(a)**) and without (**Fig. 31(b)**) BC stimulation. Comparisons between both figures follow the same trends shown in **Fig. 30**. In addition, peaks in SFP displacement amplitude occur at the same frequencies as the pressure monitors, with the exception of the open ear's peak at 3 kHz. Instead, the open ear shows an increase in SFP displacement amplitude between 1 and 4 kHz compared to the amplitude before 1 kHz. In the open ear, SFP displacement amplitude begins to significantly decrease after 4 kHz, while in the earplug cases SFP displacement decreases after 3 kHz. The CA SFP displacement peak at 0.8 kHz of approximately 70 nm is the greatest displacement amplitude shown, which is not equivalent to the pressure peak of the CA earplug, which was lower than the foam and NA earplug peaks.
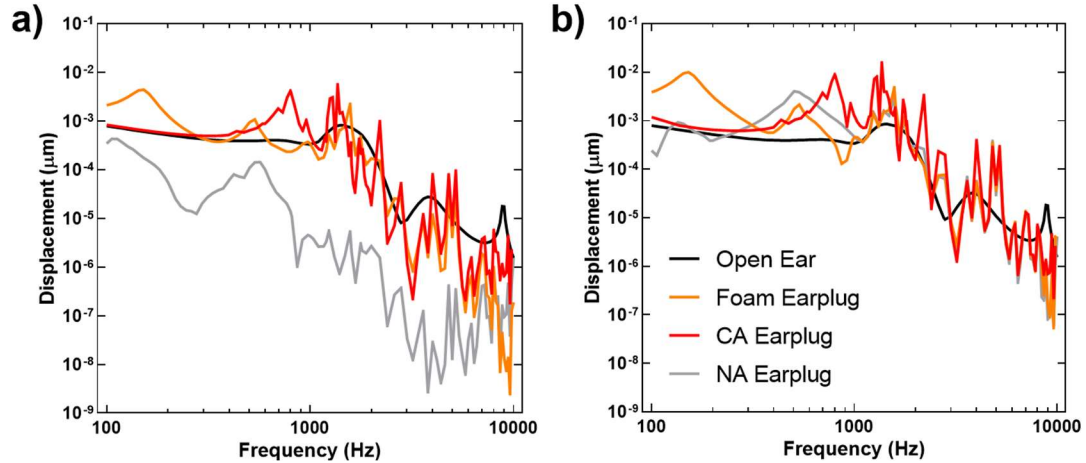
Figure 31. The FE model's predicted SFP from the harmonic acoustic analysis for the open ear, foam, CA, and experimental NA earplugs. The SFP displacement when 90 dB of acoustic pressure is applied outside of the ear canal is without (a) and with (b) BC stimulation is presented.

The results obtained from the computational model clearly demonstrate the OE when earplugs are inserted into the EC. In each model where earplugs occluded the EC, the pressure in the EC showed a significant increase. The OE dominates pressure levels below 1 kHz. When BC stimulation was applied to the model, each earplug case demonstrated a peak increase of approximately 20 dB, above the open ear case. This is a known indicator of the OE in the literature.[67,68] The increase was greatest for the foam earplug, and lowest for the CA earplug. This likely reflects the presence of the central vent in the CA plug, which helps reduce some of the pressure buildup behind the earplug. The aerogel earplug demonstrated the greatest pressure attenuation effect of the three earplugs tested, but it also showed the greatest pressure increase when BC stimulation was applied.

Comparing these results to those of Brummund et al.,[75] the foam earplug results closely approximate the same pattern of OE increase. The Brummund paper reported the maximum occluded EC pressure (and therefore the greatest pressure increase resulting from the OE) occurring at approximately 0.125 kHz, whereas for the foam earplug in this

55

study had its maximum pressure peak at approximately 0.17 kHz. Like that paper, the OE's influence gradually diminished as frequency increased, and the phenomenon did not cause a pressure increase after 1 kHz. This study builds on these results by illuminating that different materials and earplug geometries influence the nature of the OE. The aerogel earplug, which shared the geometry of the foam earplug, showed its maximum pressure peak at 0.5 kHz, demonstrating that the material plays an important role in the manifestation of this phenomenon. The CA earplug's maximum pressure peak was located at 0.8 kHz, which is likely influenced by its silicone material but may also be affected by the unique geometry of the earplug. It is notable that the order of peak pressure frequencies, from lowest to highest, corresponds with the order of the Young's moduli from lowest to highest. A more detailed analysis of the effect of occluding material on the OE might further elucidate this relationship.

This is still a preliminary study, indicated by the instability of the results in **Figs. 30** and **31**. Further work is needed to fully characterize the OE using FE modeling. The earplug materials, in particular the experimental NA earplug, need to be better described to fully account for their acoustic properties. In addition, experimental results measuring the pressure within the ear canal with earplugs inserted need to be obtained in order to verify the modeling results. In addition, deeper study into the vibration of the bony wall of the ear canal walls is needed in order to develop a better BC input. The vibration of the cartilaginous ear canal wall does not need to be measured, as the earplug seals the cartilage part of the canal, preventing it from influencing the air in the ear canal and thereby contributing to the OE.

Chapter 4: Conclusions

4.1 Research Summary and Significance

This thesis details the creation, analysis, validation, and application of a multiscale FE model of the ear canal, middle ear, cochlea, OC, and cochlear hair cells for the purposes of simulating blast wave transmission through the ear. No other studies have developed a multiscale model unifying the cochlea and hair cell models while modeling blast wave transmission. The 3-chamber cochlea developed for this model was validated against experimental measurements and improved the accuracy of the model's results. The OC model results, while still preliminary, provided some early insight into the behavior of the sensory hair cells in response to blast overpressure.

The spiral cochlea used in this FE model has 3-chambers due to the inclusion of the RM, mimicking the anatomy of the human cochlea. This led to a relative increase in the SFP displacement and decreased cochlear pressures, both of which were validated against measurements taken during blast tests. The indicates that the presence of the RM helped decrease the extremely high cochlear pressures observed in 2-chambered cochlea models. In addition, the role of the RM in cochlear biomechanics was observed to be the passive transmission of pressure from the SV to the SM. These validated results were then applied to the prediction of auditory injury, assessed using middle ear tissue strain thresholds, ARUs, and the energy entering the cochlea.

The cochlea's BM displacement peaks at 16.75 mm from the BM base were applied as input to the OC model. The preliminary results obtained from this study could not be validated against experimental measurements. The results indicated radial variation in the behavior of OHCs and HBs, and the observed bending of the HBs between the TcM and

RL in the model results resembled the "splaying out" of the stereocilia connecting both membranes observed in SEM images of blast-exposed cochleae.

Given the immense difficulty of observing the behavior of the hair cells and OC during blast wave transmission through the human ear, FE modeling is uniquely suited to predict and analyze the behavior of the OC. The integration of the microscale model of the OC with the macroscale human ear model is an important step towards fully predicting the OC behavior during blast wave transmission. The multiscale FE model of the human ear represents major progress for blast models and the understanding of the biomechanics and micromechanics of the ear.

4.2 Future Study

Several major improvements can be made to the multiscale model of the ear. Specifically, the microscale OC model will be run transiently, using the full BM displacement results predicted by the macroscale cochlea. Additionally, the documented viscoelastic material properties of some of the membranes and tissues composing the OC can be implemented into the model. Orthotropic material properties of components, including the TM and OHCs, can be applied to the model as well.

The OC behavior 16.75 mm from the base of the BM was simulated in this study. However, the BM displacement varies moving from the base to the apex of the cochlea. New models of the OC, corresponding to other locations of the BM such as the basal turn and apex, will be developed in order to observe the variation in OC behavior throughout the cochlea.

More experimental blast studies would help to further validate the model. Measurements of the BM displacement during blast wave transmission have not been

published, preventing the BM results from being validated at this time. It is an even more daunting task to measure OC motion during blast wave transmission, but doing so would enable the microscale model results to be confirmed as well.

The likelihood of injury to the ear induced by blast wave transmission was predicted using the maximum strains of the TM and ISJ, ARUs, and the energy entering the cochlea. More metrics indicating potential auditory injury should be explored and examined using the results reported by the FE model. In particular, given that the displacement and strain of the cochlear hair cells and HBs can be predicted using the OC model, the relationship between these measurements and sensorineural hearing loss should be established in order to better use the FE model to predict hearing loss. Additionally, studies assessing the quality of earplugs and other HPDs can make use of the capabilities of the FE model. More improvements to the modeling of the OE, including the BC stimulation input, earplug material properties, and measurement of the inner ear behavior when earplugs are used are necessary. Experimental measurements of the ear canal pressure and middle ear tissue displacements would enable the validation of the model's results and help the model be more reliably applied to the development of improved HPDs.

Bibliography

(1) The Office of Performance Analysis. *Veterans Benefit Administration Annual Benefits Report Fiscal Year 2022*; U.S. Department of Veterans Affairs. https://www.benefits.va.gov/REPORTS/abr/docs/2022-abr.pdf (accessed 2022-09-13).

(2) Mentel, K.; Ziriax, J.; Dachos, J.; Salunga, A.; Turner, H.; Sheffield, B.; Brungart, D. The Relationship between Speech Intelligibility and Operational Performance in a Simulated Naval Command Information Center. *Proceedings of the Human Factors and Ergonomics Society Annual Meeting* **2013**, *57* (1), 1204–1208. https://doi.org/10.1177/1541931213571268.

(3) Sheffield, B.; Brungart, D.; Blank, A. The Effects of Hearing Impairment on Fire Team Performance in Dismounted Combat. *Proceedings of the Human Factors and Ergonomics Society Annual Meeting* **2016**, *60* (1), 1509–1513. https://doi.org/10.1177/1541931213601346.

(4) Quist-Hanssen, Sv.; Thorud, E.; Aasand, G. Noise-Induced Hearing Loss and the Comprehension of Speech in Noise. *Acta Oto-Laryngologica* **1978**, *86* (sup360), 90–95. https://doi.org/10.3109/00016487809123483.

(5) Nordvik, Ø.; Laugen Heggdal, P. O.; Brännström, J.; Vassbotn, F.; Aarstad, A. K.; Aarstad, H. J. Generic Quality of Life in Persons with Hearing Loss: A Systematic Literature Review. *BMC Ear Nose Throat Disord* **2018**, *18* (1), 1–13. https://doi.org/10.1186/s12901-018-0051-6.

(6) Dougherty, A. L.; MacGregor, A. J.; Han, P. P.; Viirre, E.; Heltemes, K. J.; Galarneau, M. R. Blast-Related Ear Injuries among U.S. Military Personnel. *J Rehabil Res Dev* **2013**, *50* (6), 893–904. https://doi.org/10.1682/JRRD.2012.02.0024.

(7) Grant, K. W.; Kubli, L. R.; Phatak, S. A.; Galloza, H.; Brungart, D. S. Estimated Prevalence of Functional Hearing Difficulties in Blast-Exposed Service Members With Normal to Near–Normal-Hearing Thresholds. *Ear and Hearing* **2021**, *42* (6), 1615. https://doi.org/10.1097/AUD.0000000000001067.

(8) Stuhmiller, J. H.; Phillips, Y. Y.; Richmond, D. R. Chapter 7: THE PHYSICS AND MECHANISMS OF PRIMARY BLAST INJURY. In *Conventional Warfare: Ballistic, Blast, and Burn Injuries*; Office of the Surgeon General: Department of the Army: United States of America, 1991; pp 241–270.

(9) Jiang, S.; Smith, K.; Gan, R. Z. Dual-Laser Measurement and Finite Element Modeling of Human Tympanic Membrane Motion under Blast Exposure. *Hear. Res.* **2019**, *378*, 43–52. https://doi.org/10.1016/j.heares.2018.12.003.

(10) Jiang, S.; Dai, C.; Gan, R. Z. Dual-Laser Measurement of Human Stapes Footplate Motion under Blast Exposure. *Hear. Res.* **2021**, *403*, 108177. https://doi.org/10.1016/j.heares.2021.108177.

(11) Gan, R. Z.; Nakmali, D.; Ji, X. D.; Leckness, K.; Yokell, Z. Mechanical Damage of Tympanic Membrane in Relation to Impulse Pressure Waveform – A Study in Chinchillas. *Hear. Res.* **2016**, *340*, 25–34. https://doi.org/10.1016/j.heares.2016.01.004.

(12) Hickman, T. T.; Smalt, C.; Bobrow, J.; Quatieri, T.; Liberman, M. C. Blast-Induced Cochlear Synaptopathy in Chinchillas. *Sci. Rep.* **2018**, *8* (1), 10740. https://doi.org/10.1038/s41598-018-28924-7.

(13)   Paik, C. B.; Pei, M.; Oghalai, J. S. Review of Blast Noise and the Auditory System. *Hear. Res.* **2022**, 108459. https://doi.org/10.1016/j.heares.2022.108459.

(14)   Böhnke, F.; Arnold, W. 3D-Finite Element Model of the Human Cochlea Including Fluid-Structure Couplings. *ORL* **1999**, *61* (5), 305–310. https://doi.org/10.1159/000027688.

(15)   Kim, N.; Homma, K.; Puria, S.; Steele, C. R.; Shera, C. A.; Olson, E. S. Bone Conduction Hearing: Three-Dimensional Finite Element Model of the Human Middle and Inner Ear; Williamstown, Massachusetts (USA), 2011; pp 340–345. https://doi.org/10.1063/1.3658108.

(16)   Zhang, X.; Gan, R. Z. A Comprehensive Model of Human Ear for Analysis of Implantable Hearing Devices. *IEEE Trans. Biomed. Eng.* **2011**, *58* (10), 3024–3027. https://doi.org/10.1109/TBME.2011.2159714.

(17)   Zhang, X.; Gan, R. Z. Finite Element Modeling of Energy Absorbance in Normal and Disordered Human Ears. *Hear. Res.* **2013**, *301*, 146–155. https://doi.org/10.1016/j.heares.2012.12.005.

(18)   Elliott, S. J.; Ni, G.; Mace, B. R.; Lineton, B. A Wave Finite Element Analysis of the Passive Cochlea. *Jou. Acoust. Soc. Am.* **2013**, *133* (3), 1535–1545. https://doi.org/10.1121/1.4790350.

(19)   De Paolis, A.; Watanabe, H.; Nelson, J. T.; Bikson, M.; Packer, M.; Cardoso, L. Human Cochlear Hydrodynamics: A High-Resolution MCT-Based Finite Element Study. *Jou. Biomech.* **2017**, *50*, 209–216. https://doi.org/10.1016/j.jbiomech.2016.11.020.

(20)   Brown, M. A.; Ji, X. D.; Gan, R. Z. 3D Finite Element Modeling of Blast Wave Transmission from the External Ear to Cochlea. *Ann. Biomed. Eng.* **2021**, *49* (2), 757–768. https://doi.org/10.1007/s10439-020-02612-y.

(21)   Brown, M. A.; Bradshaw, J. J.; Gan, R. Z. Three-Dimensional Finite Element Modeling of Blast Wave Transmission From the External Ear to a Spiral Cochlea. *Jou. Biomech. Eng.* **2022**, *144* (1), 014503. https://doi.org/10.1115/1.4051925.

(22)   Gan, R. Z.; Reeves, B. P.; Wang, X. Modeling of Sound Transmission from Ear Canal to Cochlea. *Ann. Biomed. Eng.* **2007**, *35* (12), 2180–2195. https://doi.org/10.1007/s10439-007-9366-y.

(23)   Gan, R. Z.; Feng, B.; Sun, Q. Three-Dimensional Finite Element Modeling of Human Ear for Sound Transmission. *Ann. Biomed. Eng.* **2004**, *32* (6), 847–859. https://doi.org/10.1023/B:ABME.0000030260.22737.53.

(24)   Leckness, K.; Nakmali, D.; Gan, R. Z. Computational Modeling of Blast Wave Transmission Through Human Ear. *Mil. Med.* **2018**, *183* (suppl_1), 262–268. https://doi.org/10.1093/milmed/usx226.

(25)   Ramamoorthy, S.; Deo, N. V.; Grosh, K. A Mechano-Electro-Acoustical Model for the Cochlea: Response to Acoustic Stimuli. *Jou. Acoust. Soc. Am.* **2007**, *121* (5), 2758–2773. https://doi.org/10.1121/1.2713725.

(26)   Meaud, J.; Grosh, K. The Effect of Tectorial Membrane and Basilar Membrane Longitudinal Coupling in Cochlear Mechanics. *The Journal of the Acoustical Society of America* **2010**, *127* (3), 1411–1421. https://doi.org/10.1121/1.3290995.

(27)   Zagadou, B. F.; Barbone, P. E.; Mountain, D. C. Elastic Properties of Organ of Corti Tissues from Point-Stiffness Measurement and Inverse Analysis. *Jou. Biomech.* **2014**, *47* (6), 1270–1277. https://doi.org/10.1016/j.jbiomech.2014.02.025.

(28)   Sasmal, A.; Grosh, K. Unified Cochlear Model for Low- and High-Frequency Mammalian Hearing. *Proceedings of the National Academy of Sciences* **2019**, *116* (28), 13983–13988. https://doi.org/10.1073/pnas.1900695116.

(29)   Wright, A. Dimensions of the Cochlear Stereocilia in Man and the Guinea Pig. *Hear Res* **1984**, *13* (1), 89–98. https://doi.org/10.1016/0378-5955(84)90099-6.

(30)   Meenderink, S. W. F.; Shera, C. A.; Valero, M. D.; Liberman, M. C.; Abdala, C. Morphological Immaturity of the Neonatal Organ of Corti and Associated Structures in Humans. *JARO* **2019**, *20* (5), 461–474. https://doi.org/10.1007/s10162-019-00734-2.

(31)   Kolston, P. J.; Ashmore, J. F. Finite Element Micromechanical Modeling of the Cochlea in Three Dimensions. *J Acoust Soc Am* **1996**, *99* (1), 455–467. https://doi.org/10.1121/1.414557.

(32)   Motallebzadeh, H.; Soons, J. A. M.; Puria, S. Cochlear Amplification and Tuning Depend on the Cellular Arrangement within the Organ of Corti. *Proc. Natl. Acad. Sci. U.S.A.* **2018**, *115* (22), 5762–5767. https://doi.org/10.1073/pnas.1720979115.

(33)   Zetes, D. E.; Tolomeo, J. A.; Holley, M. C. Structure and Mechanics of Supporting Cells in the Guinea Pig Organ of Corti. *PLOS ONE* **2012**, *7* (11), e49338. https://doi.org/10.1371/journal.pone.0049338.

(34)   Herrmann, G.; Liebowitz, H. Chapter 10 - Mechanics of Bone Fracture. In *Fracture of Nonmetals and Composites*; Liebowitz, H., Ed.; Academic Press, 1972; pp 771–840. https://doi.org/10.1016/B978-0-12-449707-8.50014-2.

(35)   Kirikae, I. *The Structure and Function of the Middle Ear*; University of Tokyo Press: Tokyo, 1960.

(36)   Gan, R. Z.; Sun, Q.; Feng, B.; Wood, M. W. Acoustic–Structural Coupled Finite Element Analysis for Sound Transmission in Human Ear—Pressure Distributions. *Med. Eng. & Phys.* **2006**, *28* (5), 395–404. https://doi.org/10.1016/j.medengphy.2005.07.018.

(37)   Sun, Q.; Gan, R. Z.; Chang, K.-H.; Dormer, K. J. Computer-Integrated Finite Element Modeling of Human Middle Ear. *Biomech. Model. Mechanobiol.* **2002**, *1* (2), 109–122. https://doi.org/10.1007/s10237-002-0014-z.

(38)   Reichenbach, T.; Stefanovic, A.; Nin, F.; Hudspeth, A. J. Waves on Reissner's Membrane: A Mechanism for the Propagation of Otoacoustic Emissions from the Cochlea. *Cell Rep.* **2012**, *1* (4), 374–384. https://doi.org/10.1016/j.celrep.2012.02.013.

(39)   Zwislocki, J. J.; Cefaratti, L. K. Tectorial Membrane II: Stiffness Measurements in Vivo. *Hearing Research* **1989**, *42* (2), 211–227. https://doi.org/10.1016/0378-5955(89)90146-9.

(40)   Gueta, R.; Barlam, D.; Shneck, R. Z.; Rousso, I. Measurement of the Mechanical Properties of Isolated Tectorial Membrane Using Atomic Force Microscopy. *Proceedings of the National Academy of Sciences* **2006**, *103* (40), 14790–14795. https://doi.org/10.1073/pnas.0603429103.

(41)   Matsui, T.; Nakajima, C.; Yamamoto, Y.; Andoh, M.; Iida, K.; Murakoshi, M.; Kumano, S.; Wada, H. Analysis of the Dynamic Behavior of the Inner Hair Cell Stereocilia by the Finite Element Method. *JSME International Journal Series C Mechanical Systems, Machine Elements and Manufacturing* **2006**, *49* (3), 828–836. https://doi.org/10.1299/jsmec.49.828.

(42)   Sugawara, M.; Ishida, Y.; Wada, H. Local Mechanical Properties of Guinea Pig Outer Hair Cells Measured by Atomic Force Microscopy11This Study Was Presented at the 25th Midwinter Research Meeting of the Association for Research in Otolaryngology in January 2002. *Hearing Research* **2002**, *174* (1), 222–229. https://doi.org/10.1016/S0378-5955(02)00696-2.

(43)   Spector, A. A.; Brownell, W. E.; Popel, A. S. Mechanical and Electromotile Characteristics of Auditory Outer Hair Cells. *Med. Biol. Eng. Comput.* **1999**, *37* (2), 247–251. https://doi.org/10.1007/BF02513294.

(44)   Naidu, R. C.; Mountain, D. C. Longitudinal Coupling in the Basilar Membrane. *JARO* **2001**, *2* (3), 257–267. https://doi.org/10.1007/s101620010013.

(45)   Sugawara, M.; Ishida, Y.; Wada, H. Mechanical Properties of Sensory and Supporting Cells in the Organ of Corti of the Guinea Pig Cochlea – Study by Atomic Force Microscopy. *Hear. Res.* **2004**, *192* (1), 57–64. https://doi.org/10.1016/j.heares.2004.01.014.

(46)   Laffon, E.; Angelini, E. On the Deiters Cell Contribution to the Micromechanics of the Organ of Corti. *Hearing Research* **1996**, *99* (1), 106–109. https://doi.org/10.1016/S0378-5955(96)00089-5.

(47)   Tolomeo, J. A.; Holley, M. C. Mechanics of Microtubule Bundles in Pillar Cells from the Inner Ear. *Biophysical Journal* **1997**, *73* (4), 2241–2247. https://doi.org/10.1016/S0006-3495(97)78255-9.

(48)   Bien, A. G.; Jiang, S.; Gan, R. Z. Real-Time Measurement of Stapes Motion and Intracochlear Pressure during Blast Exposure. *Hear. Res.* **2023**, *429*, 108702 (pp. 1-11). https://doi.org/10.1016/j.heares.2023.108702.

(49)   Dewey, J. M. The Air Velocity in Blast Waves from t.n.t. Explosions. *Proc. Royal Soc. Lon. Ser. A. Math. Phys. Sci.* **1964**, *279* (1378), 366–385. https://doi.org/10.1098/rspa.1964.0110.

(50)   Greene, N. T.; Alhussaini, M. A.; Easter, J. R.; Argo, T. F.; Walilko, T.; Tollin, D. J. Intracochlear Pressure Measurements during Acoustic Shock Wave Exposure. *Hear. Res.* **2018**, *365*, 149–164. https://doi.org/10.1016/j.heares.2018.05.014.

(51)   Lee, J. H.; Marcus, D. C. Endolymphatic Sodium Homeostasis by REISSNER's Membrane. *Neurosci.* **2003**, *119* (1), 3–8. https://doi.org/10.1016/S0306-4522(03)00104-0.

(52)   Kim, S. H.; Kim, K. X.; Raveendran, N. N.; Wu, T.; Pondugula, S. R.; Marcus, D. C. Regulation of ENaC-Mediated Sodium Transport by Glucocorticoids in Reissner's Membrane Epithelium. **2009**, *296*, 14.

(53)   Cooper, N. P.; Rhode, W. S. Nonlinear Mechanics at the Apex of the Guinea-Pig Cochlea. *Hear. Res.* **1995**, *82* (2), 225–243. https://doi.org/10.1016/0378-5955(94)00180-X.

(54)   Niwa, K.; Mizutari, K.; Matsui, T.; Kurioka, T.; Matsunobu, T.; Kawauchi, S.; Satoh, Y.; Sato, S.; Shiotani, A.; Kobayashi, Y. Pathophysiology of the Inner Ear after Blast Injury Caused by Laser-Induced Shock Wave. *Sci Rep* **2016**, *6* (1), 31754. https://doi.org/10.1038/srep31754.

(55)   Gan, R. Z.; Jiang, S. Surface Motion Changes of Tympanic Membrane Damaged by Blast Waves. *Jou. Biomech. Eng.* **2019**, *141* (9), 091009. https://doi.org/10.1115/1.4044052.

(56)   Liu, W.; Atturo, F.; Aldaya, R.; Santi, P.; Cureoglu, S.; Obwegeser, S.; Glueckert, R.; Pfaller, K.; Schrott-Fischer, A.; Rask-Andersen, H. Macromolecular Organization and Fine Structure of the Human Basilar Membrane - RELEVANCE for Cochlear Implantation. *Cell Tissue Res* **2015**, *360* (2), 245–262. https://doi.org/10.1007/s00441-014-2098-z.

(57)   Olson, E. S.; Duifhuis, H.; Steele, C. R. Von Békésy and Cochlear Mechanics. *Hearing Research* **2012**, *293* (1), 31–43. https://doi.org/10.1016/j.heares.2012.04.017.

(58)   Cheng, T.; Dai, C.; Gan, R. Z. Viscoelastic Properties of Human Tympanic Membrane. *Ann. Biomed. Eng.* **2007**, *35* (2), 305–314. https://doi.org/10.1007/s10439-006-9227-0.

(59)   Luo, H.; Jiang, S.; Nakmali, D. U.; Gan, R. Z.; Lu, H. Mechanical Properties of a Human Eardrum at High Strain Rates After Exposure to Blast Waves. *J. dynamic behavior mater.* **2016**, *2* (1), 59–73. https://doi.org/10.1007/s40870-015-0041-3.

(60)   Zhang, X.; Gan, R. Z. Experimental Measurement and Modeling Analysis on Mechanical Properties of Incudostapedial Joint. *Biomech. Model. Mechanobiol.* **2011**, *10* (5), 713–726. https://doi.org/10.1007/s10237-010-0268-9.

(61)   Jiang, S. MECHANICAL PROPERTIES OF HUMAN INCUDOSTAPEDIAL JOINT AND TYMPANIC MEMBRANE IN NORMAL AND BLAST-DAMAGED EARS. **2018**.

(62)   Price, G. R. Validation of the Auditory Hazard Assessment Algorithm for the Human with Impulse Noise Data. *Jou. Acoust. Soc. Am.* **2007**, *122* (5), 2786. https://doi.org/10.1121/1.2785810.

(63)   Fedele, P. D.; Binseel, M. S.; Kalb, J. T.; Price, G. R. Using the Auditory Hazard Assessment Algorithm for Humans (AHAAH) With Hearing Protection Software, Release MIL-STD-1474E.

(64)   De Paolis, A.; Bikson, M.; Nelson, J. T.; de Ru, J. A.; Packer, M.; Cardoso, L. Analytical and Numerical Modeling of the Hearing System: Advances towards the Assessment of Hearing Damage. *Hear. Res.* **2017**, *349*, 111–128. https://doi.org/10.1016/j.heares.2017.01.015.

(65)   Zagadou, B.; Chan, P.; Ho, K.; Shelley, D. Impulse Noise Injury Prediction Based on the Cochlear Energy. *Hearing Research* **2016**, *342*, 23–38. https://doi.org/10.1016/j.heares.2016.02.017.

(66)   Gan, R. Z.; Leckness, K.; Smith, K.; Ji, X. D. Characterization of Protection Mechanisms to Blast Overpressure for Personal Hearing Protection Devices – Biomechanical Measurement and Computational Modeling. *Mil. Med.* **2019**, *184* (Supplement_1), 251–260. https://doi.org/10.1093/milmed/usy299.

(67)   Stenfelt, S.; Wild, T.; Hato, N.; Goode, R. L. Factors Contributing to Bone Conduction: The Outer Ear. *The Journal of the Acoustical Society of America* **2003**, *113* (2), 902–913. https://doi.org/10.1121/1.1534606.

(68)   Schroeter, J.; Poesselt, C. The Use of Acoustical Test Fixtures for the Measurement of Hearing Protector Attenuation. Part II: Modeling the External Ear, Simulating Bone Conduction, and Comparing Test Fixture and Real-ear Data. *The Journal of the Acoustical Society of America* **1986**, *80* (2), 505–527. https://doi.org/10.1121/1.394046.

(69)   Carillo, K.; Doutres, O.; Sgard, F. Theoretical Investigation of the Low Frequency Fundamental Mechanism of the Objective Occlusion Effect Induced by Bone-Conducted Stimulation. *The Journal of the Acoustical Society of America* **2020**, *147* (5), 3476–3489. https://doi.org/10.1121/10.0001237.

(70)   Fausti, S. A.; Wilmington, D. J.; Gallun, F. J.; Myers, P. J.; Henry, J. A. Auditory and Vestibular Dysfunction Associated with Blast-Related Traumatic Brain Injury. *JRRD* **2009**, *46* (6), 797. https://doi.org/10.1682/JRRD.2008.09.0118.

(71)   Kim, H. J.; Oh, S. Y.; Won, S. Y.; Kim, H. J.; Kim, T. K.; Ko, B. C.; Woo, S. Y.; Park, E.-C. Associations between Earplug Use and Hearing Loss in ROK Military Personnel. *BMJ Mil Health* **2021**, *167* (6), 398–401. https://doi.org/10.1136/jramc-2019-001378.

(72)   Soderlund, L. L.; McKenna, E. A.; Tastad, K.; Paul, M. Prevalence of Permanent Threshold Shifts in the United States Air Force Hearing Conservation Program by Career Field, 2005–2011. *Journal of Occupational and Environmental Hygiene* **2016**, *13* (5), 383–392. https://doi.org/10.1080/15459624.2015.1123814.

(73)   Moon, S. Noise-Induced Hearing Loss Caused by Gunshot in South Korean Military Service. *Military Medicine* **2007**, *172* (4), 421–425. https://doi.org/10.7205/MILMED.172.4.421.

(74)   Yankaskas, K. Prelude: Noise-Induced Tinnitus and Hearing Loss in the Military. *Hearing Research* **2013**, *295*, 3–8. https://doi.org/10.1016/j.heares.2012.04.016.

(75)   Brummund, M. K.; Sgard, F.; Petit, Y.; Laville, F. Three-Dimensional Finite Element Modeling of the Human External Ear: Simulation Study of the Bone Conduction Occlusion Effect. *The Journal of the Acoustical Society of America* **2014**, *135* (3), 1433–1444. https://doi.org/10.1121/1.4864484.

Appendix

Appendix 1. List of Abbreviations

3D: three dimensional
AHAAH: auditory hazard assessment algorithm for humans
ARU: auditory risk unit
BM: basilar membrane
BC: bone conduction
BOP: blast overpressure
CA: combat arms
CAS: central auditory system
CP: cochlear pressure
DC: Dieters' cell
FE: finite element
FSI: fluid-structure interaction
HB: hair bundle
HC: Hensen's cell
HPD: hearing protection device
IHC: inner hair cell
IPC: inner pillar cell
LDV: laser Doppler vibrometer
OC: organ of Corti
OE: occlusion effect
OHC: outer hair cell
OPC: outer pillar cell
OSL: osseous spiral lamina
OWM: oval window membrane
PAS: peripheral auditory system
PhP: phalangeal process
RL: reticular lamina
RM: Reissner's membrane
RWM: round window membrane
SFP: stapes footplate
SM: scala media
ST: scala tympani
SV: scala vestibuli
TB: temporal bone
TM: tympanic membrane
TcM: tectorial membrane